

RO2

# FINAL REPORT FOR PHASE I

RECEIVED

JAN 05 2001

OSTI

## HIGH PRODUCTIVITY VACUUM BLASTING SYSTEM

DE-AR26-98FT40367

Principal Investigator:

William S. McPhee

Florida International University  
Collaborators

M.A. Ebadian, Ph.D., and C.X. Lin, Ph.D.

Submitted by William S. McPhee

LTC TELETRAK, Inc.

ACQUISITION & ASSISTANCE  
1999 JUL 26 1 A 10: 04  
USDOE-FETC

## **DISCLAIMER**

This report was prepared as an account of work sponsored by an agency of the United States government. Neither the United States government nor any agency thereof, nor any of their employees, nor any of its contractors, subcontractors, nor their employees makes any warranty, express or implied, or assumes any legal liability or responsibility for the accuracy, completeness, or usefulness of any information, apparatus, product, or process disclosed, or represents that its use would not infringe upon privately owned rights. Reference herein to any specific commercial product, process, or service by trade name, trademark, manufacturer, or otherwise does not necessarily constitute or imply its endorsement, recommendation, or favoring by the United States government or any other agency thereof. The views and opinions of authors expressed herein do not necessarily state or reflect those of the United States government or any agency thereof.

## **DISCLAIMER**

**Portions of this document may be illegible in electronic image products. Images are produced from the best available original document.**

# **HIGH PRODUCTIVITY VACUUM BLASTING SYSTEM**

## **Principal Investigator**

**William S. McPhee**  
LTC TELETRAK, Inc.  
22446 Davis Drive, Suite 142  
Sterling, VA 20164

## **Florida International University Collaborators**

**M.A. Ebadian, Ph.D., and C.X. Lin, Ph.D.**  
Hemispheric Center for Environmental Technology  
Florida International University  
Miami, FL 33174

**May 1999**

## **Submitted by**

LTC TELETRAK, Inc.  
22446 Davis Drive, Suite 142  
Sterling, VA 20164  
Ph: 800-822-2332  
Fax: 703-406-4523

Under Grant No.: DE-AR26-98FT40367

## TABLE OF CONTENTS

---

LIST OF FIGURES .....	ii
LIST OF TABLES .....	iv
EXECUTIVE SUMMARY .....	v
OBJECTIVE .....	v
SCOPE OF WORK.....	v
TASKS PERFORMED.....	v
INTRODUCTION .....	1
PART 1. NUMERICAL MODELING .....	2
1.1 Two-phase mathematical model.....	2
1.2 Numerical results and discussion (blasting nozzles) .....	5
1.3 Numerical results and discussion (dust separators).....	13
1.4 Numerical results and discussion (wind curtain).....	17
PART 2. NEW DESIGN FOR RECTANGULAR NOZZLE, CENTRIFUGAL SEPARATOR, BLASTHEAD/ WIND CURTAIN, AND BLASTHEAD SENSOR .....	21
2.1 The design of the new rectangular nozzle .....	21
2.2 The design of new centrifugal separator.....	22
2.3 The design of the new blasthead/wind curtain with ¼ inch equivalent diameter nozzle .....	23
2.4 Blasthead sensors.....	24
PART 3. MODEL TEST.....	30
3.1. Experimental results and their comparison with CFD modeling on the blasting nozzle .....	30
3.2 Centrifugal separator test results .....	44
CONCLUSION.....	48

APPENDIX A. AutoCAD drawing for the rectangular nozzle

APPENDIX B. AutoCAD drawing for the new centrifugal separator

APPENDIX C. AutoCAD drawing for the wind curtain

## LIST OF FIGURES

---

Figure 1.	Multi-block structured grid of the existing round nozzle (the total cells are about 35,000). .....	6
Figure 2.	Particles distribution at exit plane of the existing round nozzle. ....	7
Figure 3.	Structured grid of the rectangular nozzle (total cells are about 35,000). ....	8
Figure 4.	Particle velocities on the exit plane of the rectangular nozzle (1/4" equivalent throat diameter). ....	9
Figure 5.	Particle velocities on the exit plane of the rectangular nozzle (3/8 inch equivalent throat diameter). ....	10
Figure 6.	Particles distribution at exit plane of the nozzle. ....	12
Figure 7.	Particle distribution at exit plane of the nozzle. ....	13
Figure 8.	The geometry and air flow field of the existing separator. ....	14
Figure 9.	The grid system of the new centrifugal separator. ....	15
Figure 10.	Air flow field on two symmetrical planes of the centrifugal separator. ....	16
Figure 11.	Outside diameter versus efficiency of centrifugal separator. ....	17
Figure 12.	Proposed geometry of wind curtain. ....	18
Figure 13.	Air flow field on the proposed wind curtain (gap=1/16 inch, angle = 60°, working distance = 0.25 inch). ....	19
Figure 14.	Assumed working distances versus the wind curtain efficiency at different injection pressures. ....	20
Figure 15.	AutoCAD drawing of the newly designed nozzle. ....	22
Figure 16.	Newly designed centrifugal separator. ....	23
Figure 17.	Newly designed blasthead with 0.25 inch equivalent diameter. ....	24
Figure 18.	Radiological characterization electronics. ....	26
Figure 19.	Possible arrangement of sensor component with compact blasthead chamber design. ....	27
Figure 20.	Possible arrangement of sensor components with large blasting chamber design. ....	28
Figure 21.	Radiological transducer assemblies. ....	29
Figure 22.	Electronic/indicator POD. ....	29
Figure 23.	Experimental setup of particle velocity and concentration measurement of the blasting nozzle. ....	38
Figure 24.	Measurement mechanism of the particle velocity and concentration. ....	39

Figure 25. Measurement arrangement for the existing circular nozzle with ¼ inch throat diameter.....	39
Figure 26. Measurement arrangement for the new rectangular nozzle with long side at horizontal position. ....	40
Figure 27. Measurement arrangement for the new rectangular nozzle with long side at vertical position. ....	40
Figure 28. The test section for measuring blasting nozzle velocity and construction.....	41
Figure 29. Particles imaging for circular nozzle at P =83 psi.....	41
Figure 30. Particles imaging for rectangular nozzle at P =82 psi (nozzle orientation, see Figure 26).....	42
Figure 31. Particles imaging for rectangular nozzle at P =65 psi (nozzle orientation, see Figure 26).....	42
Figure 32. Particles imaging for rectangular nozzle at P =82 psi (nozzle orientation, see Figure 27).....	43
Figure 33. Particles imaging for rectangular nozzle at P =65 psi (nozzle orientation, see Figure 27).....	43
Figure 34. Picture of the new centrifugal separator.....	45
Figure 35. Comparison of numerical results and experiment data in the axial direction at the upper position (i.e., 2" to the separator's top surface).....	46
Figure 36. Comparison of numerical results and experiment data in the tangential direction at the upper position (i.e., 2" to the separator's top surface).....	46
Figure 37. Comparison of numerical results and experiment data in the axial direction at the lower position (i.e., 6" to the separator's top surface).....	47
Figure 38. Comparison of numerical results and experiment data in the tangential direction at the lower position (i.e., 6" to the separator's top surface).....	47

## LIST OF TABLES

---

Table 1. The average particle velocities at the exit plane of the rectangular nozzle.....	11
Table 2. The average particle velocities at exit plane of the rectangular nozzle.....	13
Table 3. Comparison of the efficiency of two separators.....	15
Table 4. Flow passage dimensions of the rectangular nozzle ( $\frac{1}{4}$ - inch equivalent diameter) .....	21
Table 5. Six test cases.....	32
Table 6. Typical data points of grit velocity measurement (existing round nozzle, $\frac{1}{4}$ inch, pressure=83 psi).....	32
Table 7. Typical data points of grit velocity measurement (existing round nozzle, $\frac{1}{4}$ inch, pressure=65 psi).....	34
Table 8. Typical data points of grit velocity measurement (the new rectangular nozzle, $\frac{1}{4}$ inch equivalent diameter, pressure=82 psi) .....	35
Table 9. Typical data points of grit velocity measurement (the new rectangular nozzle, $\frac{1}{4}$ inch equivalent diameter, pressure=65 psi) .....	36
Table 10. Comparison of the measurement results with CFD modeling data.....	37
Table 11. Comparison of the measurement results with CFD modeling data.....	44



## EXECUTIVE SUMMARY

---

### OBJECTIVE

The objective of this project is to improve the productivity and lower the expense of existing vacuum blasting technology. This technology is used to remove radioactive contamination, PCBs, and lead-based paint and provides worker protection by continuously recycling the material and dust for the decontamination tasks. The proposed work would increase the cleaning rate and provide safe and cost-effective decontamination of the DOE sites.

### SCOPE OF WORK

This work focuses on redesigning and improving existing vacuum blasting technology including blast head nozzles, ergonomic handling of the blast head by reducing its weight; brush-ring design, vacuum level regulator, efficiency of the dust separator, and operational control sensors. The redesign is expected to enhance the productivity and economy of the vacuum blasting system by at least 50 percent over current vacuum blasting systems.

There are three phases in the project. Phase I consists of developing and testing mathematical models. Phase II consists of pre-prototype design and fabrication and pre-prototype unit testing. Phase III consists of prototype design and field verification testing.

In phase I, mathematical models are developed and analyzed for the nozzle, blast head, wind curtain, and dust separator, first as individual devices and then combined as an integrated model. This allows study of respective airflow and design parameters. The Contractor shall, based on the results of the mathematical modeling studies, design experimental models of the components and test these models. In addition, the Contractor shall develop sensors to detect the relationship of the blast head to the blast surfaces and controls to minimize the dependency on an operator's skill and judgment to obtain optimum positioning, as well as real-time characterization sensors to determine as the blast head is moving the depth to which coatings must be removed, thereby improving production and minimizing waste.

In phase II, the Contractor shall design and construct a pre-prototype of the nozzle, blast head with wind curtain, sensors, and dust separator and test this system to assess the performance of the new design under controlled conditions at the contractor's facility.

In phase III, the Contractor shall design and construct a prototype of the High Productivity Vacuum Blasting System, based on the results of the pre-prototype design and testing performed. This unit will be a full-scale prototype and will be tested at a designated Department of Energy (DOE) facility. Based on the results, the system performance, the productivity, and the economy of the improved vacuum blasting system will be evaluated.

### TASKS PERFORMED

This report deals with Phase I only. In order to meet the needs of phase I, first we developed mathematical models and related code to simulate the entire process numerically. Second, based on the modeling data, we designed, manufactured, and finally tested an innovative rectangular

nozzle and a new centrifugal separator. The model shows that the experimental results agree with the numerical estimated data with a deviation within  $\pm 10\%$ , thus proving the mathematical model and the model test successful.

For the mathematical models, a series of numerical methods are developed to simulate the air-particle flow in the entire vacuum blasting system, which includes air-particle flow in nozzle, separator, and wind curtain. Based on the numerical data and mechanical view, the innovative rectangular nozzle and a new centrifugal separator are proposed to replace the existing round nozzle and separator. Optimum geometric and operative parameters for every component of the vacuum blasting system are proposed. The numerical results show that the productivity and economy of the existing vacuum system can be increased by 50 percent when the recommended configuration of nozzle and separator are used.

The model test of the nozzle and separator are performed to verify the mathematical models. For the nozzle, the particle velocity and distribution on the exit plane of the nozzle are measured by a high-speed video camera system. For the separator, efficiency is measured by the existing LTC machine; the separator's internal velocity distribution is measured by Pitot probe. The numerical results agree with the measured data with a deviation within  $\pm 10\%$ . Experimental results also show that if the new innovative design rectangular nozzle replaces the old circular nozzle, more than a 50 percent increase in productivity efficiency can be achieved. The newly designed centrifugal separator offers a high-efficiency separation increase from about 30 percent to 75 percent, even using finer abrasives.

Two types of blasthead sensor systems, a radiological characterization sensor system and a lift-off sensor system, are proposed and discussed. The radiological characterization sensor system will be incorporated into the structure of the blast head as compactly as possible to minimize the standoff distance from an adjacent perpendicular surface. The lift-off sensor system will incorporate sensitive differential pressure switches/transducers to monitor the generated negative pressure within the blasthead. Additionally, based on numerical data and a mechanical view, a new blasting head and wind curtain have been also designed.

## INTRODUCTION

---

The Department of Energy (DOE) needs improved technologies to decontaminate large areas of both concrete and steel surfaces. The technology should have high operational efficiency, minimize exposures to workers, and produce low levels of secondary waste.

In order to meet the DOE needs, an applied research and development project for the improvement of a currently used decontamination technology, Vacuum Blasting, is proposed by implementing an innovative design of nozzle, blasthead, and dust separator. The proposed work will increase the cleaning rate and provide safe and cost-effective decontamination of the DOE sites. The redesign is expected to enhance the productivity and economy of the vacuum blasting system by at least 50 percent over the current vacuum blasting system.

Recent research for the open blasting industry has shown that the performance of the nozzle can be improved in three ways: 1) run at the design nozzle pressure or above; 2) run the smallest feasible abrasive grit size; 3) use an improved blasting nozzle. Among these three, only the redesign of the nozzle offers an estimated 80 percent increase in efficiency. Work done recently has achieved an order-of-magnitude increase in the overall performance of blasting nozzles. With a better understanding of the air-abrasive flow inside the nozzles as well as inside the blasthead, a better vacuum blasting nozzle should be developed.

The second job to be considered is the dust separator. Present operating experience with the LTC Vacuum Blasting Machine shows that the separation performance is not satisfactory for small size grit. Fine steel grit particles are useful for improving the cleaning production rate. However, such fine particles are easily entrained by the fine particles and the dust removed from the decontamination surfaces. This decreases the efficiency of the whole system. The dust separator will be redesigned or a secondary separator introduced based upon testing.

The new blasthead will also need to incorporate sensors for triggering shut-down if the blasthead is taken from the surface. Also sensors to ensure neither "under or over" cleaning of a given surface area by providing highly desirable real-time characterization to determine the effectiveness of decontamination. The sensors to meet such demands will be developed.

The entire project consists of three phases. Phase I develops and tests mathematical models. Phase II consists of pre-prototype design and fabrication and pre-prototype unit testing. Phase III consists of prototype design and field verification testing. This report deals with the first phase only. The main objective of this phase is to develop and test a mathematical model for a high production vacuum blasting system, using an existing LTC machine as the base criterion.

In order to meet the need of phase I, we first developed mathematical models and related code to simulate the entire process numerically. Second, based on the modeling data, we designed, manufactured, and finally tested an innovative rectangular nozzle and a new centrifugal separator. The experimental results agreed with the numerical estimated data with a deviation within  $\pm 10\%$ , thus proving the mathematical model and the model test successful.

## PART 1. NUMERICAL MODELING

---

### 1.1 Two-phase mathematical model

The fully three-dimensional air-particle two-phase model, incorporating some existing models, has been developed for simulating two-phase flow in the entire vacuum blasting system. The calculations were performed for the blasting nozzle, separator, and blasthead/wind curtain. The governing equations, turbulent models, and boundary conditions, etc., are described in detail in the following sections.

#### 1.1.1 Governing equations for continuous phase

For the continuous phase (compressible air), the governing equations for conservation of mass, momentum, and energy can be written as follows:

Mass:

$$\frac{\partial \rho}{\partial t} + \frac{\partial(\rho u_i)}{\partial x_i} = 0 \quad (1)$$

Momentum:

$$\frac{\partial}{\partial t}(\rho u_i) + \frac{\partial}{\partial x_j}(\rho u_i u_j + p) - \frac{\partial \tau_{ij}}{\partial x_j} = 0 \quad (2)$$

Energy:

$$\frac{\partial e}{\partial t} + \frac{\partial}{\partial x_j}(u_j(e + p)) - \frac{\partial}{\partial x_j}(u_i \tau_{ji} + q_j) = 0 \quad (3)$$

With the assumptions of ideal air, the following additional equations can be added to correlate the governing equations.

State equation:

$$p = \rho RT \quad (4)$$

For energy  $e$ , we have

$$e = \frac{p}{\gamma - 1} + \frac{1}{2}(u_1^2 + u_2^2 + u_3^2) \quad (5)$$

Because the air velocity is not very high in some region of the vacuum blasting system, such as in separator and head of blasthead, the air can be considered as an incompressible fluid in those regions. Thus, the governing equations for incompressible flow can be simplified as the following:

Mass:

$$\frac{\partial u_i}{\partial x_i} = 0 \quad (6)$$

Momentum:

$$\frac{\partial}{\partial x_j} (u_i u_j + p) - \frac{\partial \tau_{ij}}{\partial x_j} = 0 \quad (7)$$

### 1.1.2 Turbulence models for continuous phase

The standard  $k-\varepsilon$  model was adopted in this study. This turbulence model contains the transport model equation considering the turbulent kinetic energy ( $k$ ) and its dissipation rate ( $\varepsilon$ ). The  $k$  equation was derived from the exact equation, while the  $\varepsilon$  equation was obtained using physical reasoning and bears little resemblance to its mathematically exact counterpart.

The turbulent kinetic energy,  $k$ , and its rate of dissipation,  $\varepsilon$ , were obtained from the following transport equations:

$$\rho \frac{Dk}{Dt} = \frac{\partial}{\partial x_i} \left[ \left( \mu + \frac{\mu_t}{\sigma_k} \right) \frac{\partial k}{\partial x_i} \right] + G_k + G_b - \rho \varepsilon - Y_M \quad (8)$$

and

$$\rho \frac{D\varepsilon}{Dt} = \frac{\partial}{\partial x_i} \left[ \left( \mu + \frac{\mu_t}{\sigma_\varepsilon} \right) \frac{\partial \varepsilon}{\partial x_i} \right] + C_{1\varepsilon} \frac{\varepsilon}{k} (G_k + C_{3\varepsilon} G_b) - C_{2\varepsilon} \rho \frac{\varepsilon^2}{k} \quad (9)$$

where  $G_k$  represents the generation of turbulent kinetic energy due to mean velocity gradients,  $G_b$  is the generation of turbulent kinetic energy due to buoyancy,  $Y_M$  represents the contribution of the fluctuating dilatation in compressible turbulence to the overall dissipation rate, and  $C_{1\varepsilon}$ ,  $C_{2\varepsilon}$ , and  $C_{3\varepsilon}$  are constants.  $\sigma_k$  and  $\sigma_\varepsilon$  are the turbulent Prandtl numbers for  $k$  and  $\varepsilon$ , respectively.

### 1.1.3 Force balance equations for discrete phase

The discrete phase (particle) was simulated in a Lagrangian frame of reference. The discrete phase consisted of spherical particles dispersed in the continuous phase (air). The trajectory of the discrete phase particle was predicted by integrating the force balance on the particle, which was written in a Lagrangian reference frame. This force balance equated the particle inertia with

the forces acting on the particle and can be written (for the x direction in Cartesian coordinates) as

$$\frac{du_p}{dt} = F_D(u - u_p) + g_x(\rho_p - \rho) / \rho_p \quad (10)$$

where  $F_D(u - u_p)$  was the drag force per unit particle mass and

$$F_D = \frac{18\mu}{\rho_p D_p^2} \frac{C_D \text{Re}}{24} \quad (11)$$

where  $u$  is the fluid phase velocity,  $u_p$  is the particle velocity,  $\mu$  is the molecular viscosity of the fluid,  $\rho$  is the fluid density,  $\rho_p$  is the density of the particles, and  $D_p$  is the particle diameter. Re is the relative Reynolds number, which is defined as

$$\text{Re} = \frac{\rho D_p |u_p - u|}{\mu} \quad (12)$$

The drag coefficient,  $C_D$ , is a function of the relative Reynolds number of the following general forms:

$$C_D = a_1 + a_2 / \text{Re} + a_3 / \text{Re}_2 \quad (13)$$

where  $a_1$ ,  $a_2$  and  $a_3$  are the constants that apply for smooth spherical particles over several ranges of Re.

#### 1.1.4 Discrete phase in turbulent flows

The dispersion of particles due to turbulence in the fluid phase is modeled using the stochastic discrete-particle approach. In this approach, the turbulent dispersion of particles is predicted by integrating the trajectory equations for individual particles, using the instantaneous fluid velocity,  $\bar{u} + u'(t)$ , along the particle path during the integration. Computing the trajectory in this manner for a sufficient number of representative particles may account for the random effects of turbulence on the particle dispersion. In this study, the Discrete Random Walk (DRW) model is used. In this model, the fluctuation velocity components are discrete piecewise constant functions of time. Their random values are kept constant over an interval of time given by the characteristic.

#### 1.1.5 Performing trajectory of discrete phase calculation

In the uncoupled two-phase flow calculation, the following steps were performed:

- The continuous phase flow field was calculated.
- The discrete phase was introduced by computing the particle trajectories for each discrete phase injection.

### *1.1.6 Boundary conditions*

There are two sets of boundary conditions. The first one is for the continuous phase (air); the second is for the discrete phase (particle).

For the continuous phase (air), a non-slip boundary condition was imposed on the wall. The total pressure, temperature, and static pressure were known at the nozzle entrance. At the nozzle exit plane, all flow quantities were extrapolated from the two neighboring interior planes upstream of the exit plane. For separator and blasthead/wind curtain, the velocity inlet and pressure outlet boundary conditions were imposed on inlet and outlet plane.

For the discrete phase (particle), the available boundary conditions included the following:

“Reflect” indicates the rebound of the particle from the boundary in question with a change in its momentum being defined by the coefficient of restitution. For these computations, a coefficient of restitution equal to 0.0 implied that the particle retained none of its normal momentum after the rebound. A coefficient of restitution equal to 1.0 implied that the particle retained all of its normal momentum after the rebound (an elastic collision).

“Trap” indicates the termination of the trajectory calculations, and the fate of the particle is recorded as “trapped.”

“Escape” indicates the particle as having “escaped” when it encounters the boundary in question, thereby terminating trajectory calculations.

In this study, the following discrete phase boundary conditions were adopted:

- Inlet: “Escape”
- Outlet: “Escape”
- Wall: “Reflect,” a coefficient of restitution equal to 1.0

### *1.1.7 Particle physics properties*

Two kinds of standard steel grits were adapted in this study: G40 with a particle size of 820  $\mu\text{m}$ , and G80 with a particle size of 300  $\mu\text{m}$ . Both have the specific gravity of 7.0  $\text{g}/\text{cm}^3$ .

## **1.2 Numerical results and discussion (blasting nozzles)**

### *1.2.1 Numerical results on the existing round nozzle*

The calculations were performed with the fully three-dimensional model. The particle concentration distribution at the exit plane was obtained. Figure 1 shows the grid generation of the existing round nozzle with a throat diameter of  $\frac{1}{4}$  inch. Several cases for different inlet pressure have been run. When the nozzle inlet pressure was 100 Psi, the statistic average particle velocities on the exit plane of the nozzle were just 45m/s for G40 steel grit and 70 m/s for G80 steel grit, probably because the nozzle is too short to provide enough residence time for the steel grit in the nozzle. This is one of the major disadvantages.

The particle distribution at the exit plane of the nozzle is shown in Figure 2. When blasting, the steel particles were too concentrated, resulting in a narrow particle beam with a diameter of 0.46 inch (in a total circular area with a diameter of 0.72 inch). This is the second major disadvantage.

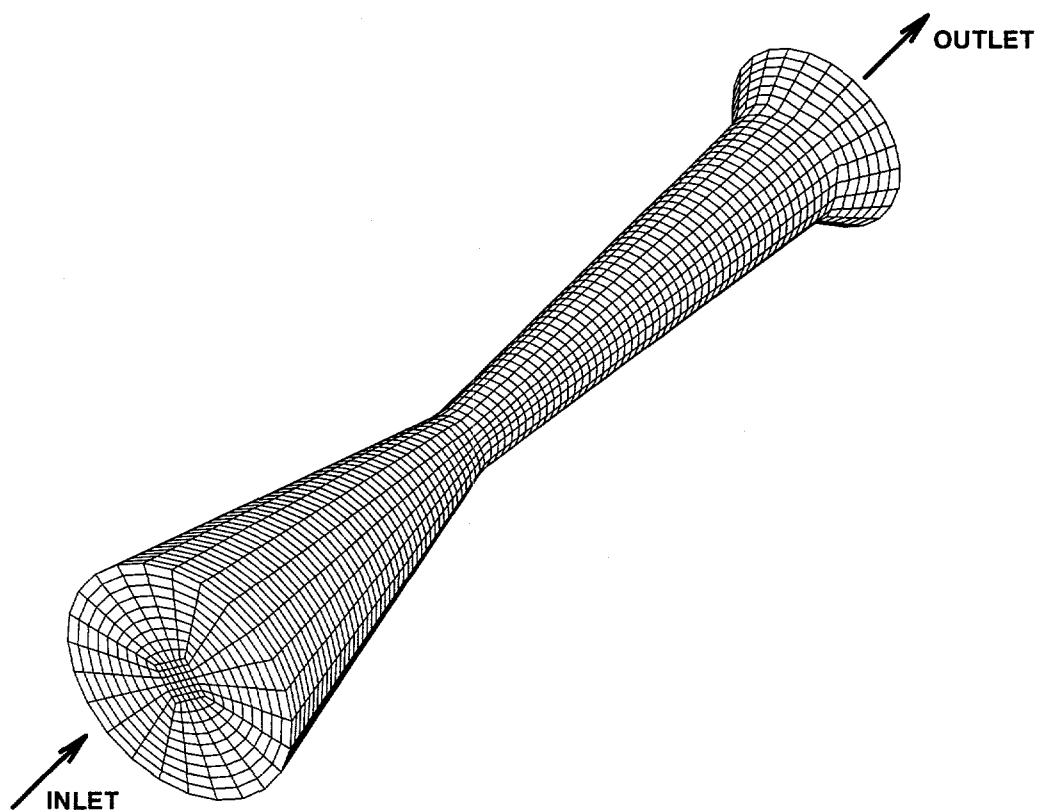


Figure 1. Multi-block structured grid of the existing round nozzle (the total cells are about 35,000).



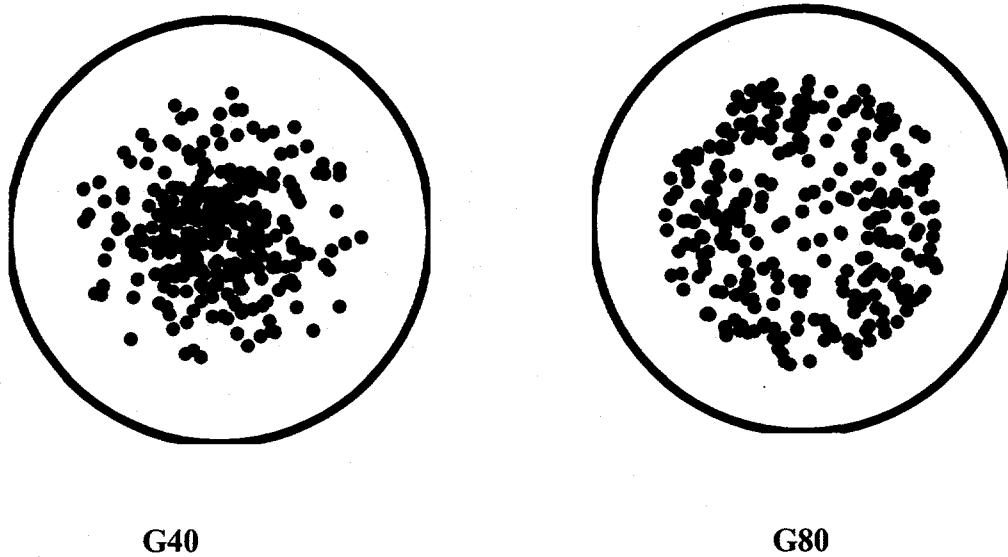


Figure 2. Particles distribution at exit plane of the existing round nozzle.

### 1.2.2 Numerical results on the new rectangular nozzle

There are two major disadvantages of the existing round nozzle. One is lower particle velocity, and the other is the concentrated particle distribution. The two disadvantages greatly limit the blasthead cleaning rate. The main reasons are that the length of the round nozzle is too short (3.86 inch, see table 4 for details) and the structure of the round nozzle is not optimum. Although the blasthead cleaning rate can be increased by increasing the length of the existing round nozzle, theoretically there still exists other substantial disadvantages in the configuration of the round nozzle.

In this project, the new rectangular nozzle was proposed to overcome the disadvantages of the existing round nozzle. The new rectangular nozzle also provided convenient for redesigning the entire vacuum blasting system which will be discussed later. The geometry and grid system of the new rectangular nozzle is shown in Figure 3. Two kinds of rectangular nozzles with 1/4 and 3/8 inch equivalent throat diameters were calculated for different lengths. The objective is to verify how the nozzle length affects the velocity and particle distribution and choose a suitable length. The theory is that increasing the nozzle length results in long resident time of the particles in the nozzle and increases the particle velocity. These cases are obtained with the same conditions. Figure 4 shows the particle velocity at nozzle exit plane versus nozzle divergent length for 1/4 inch equivalent throat diameter. A slop increase of the velocity with increasing the length is obtained when the divergent length is less than 8~10 inches. However, a slow increase trend is obtained when the length is larger than 8~10 inches. Such a trend is similar for both G-40 and G-80 particle grit. Figure 5 shows the results for 3/8 inch equivalent throat diameter. The particle velocities are higher than those with 1/4 inch equivalent diameter.

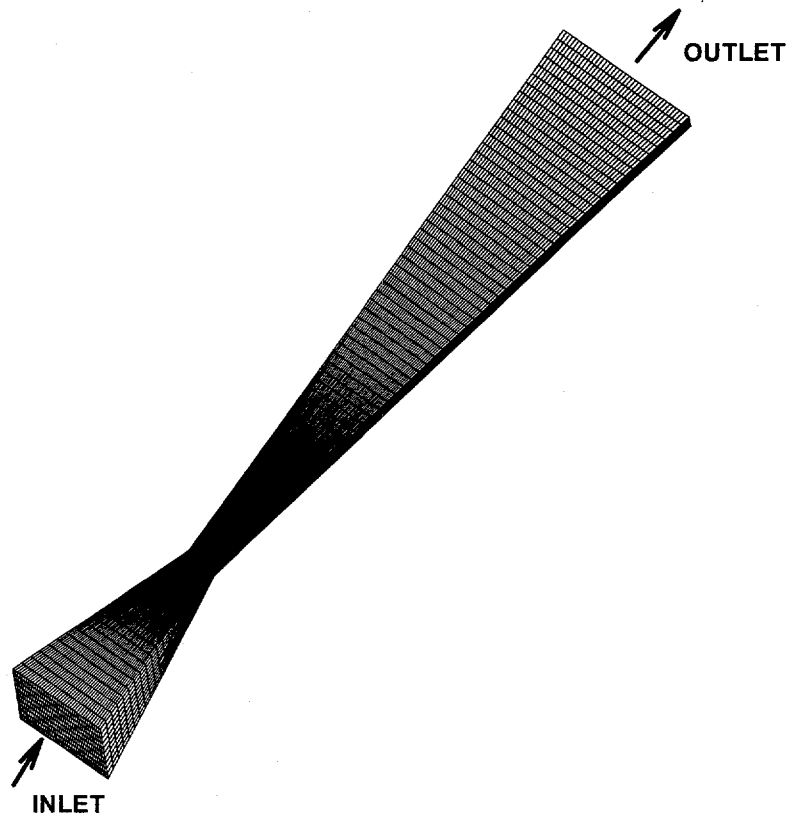


Figure 3. Structured grid of the rectangular nozzle (total cells are about 35,000).

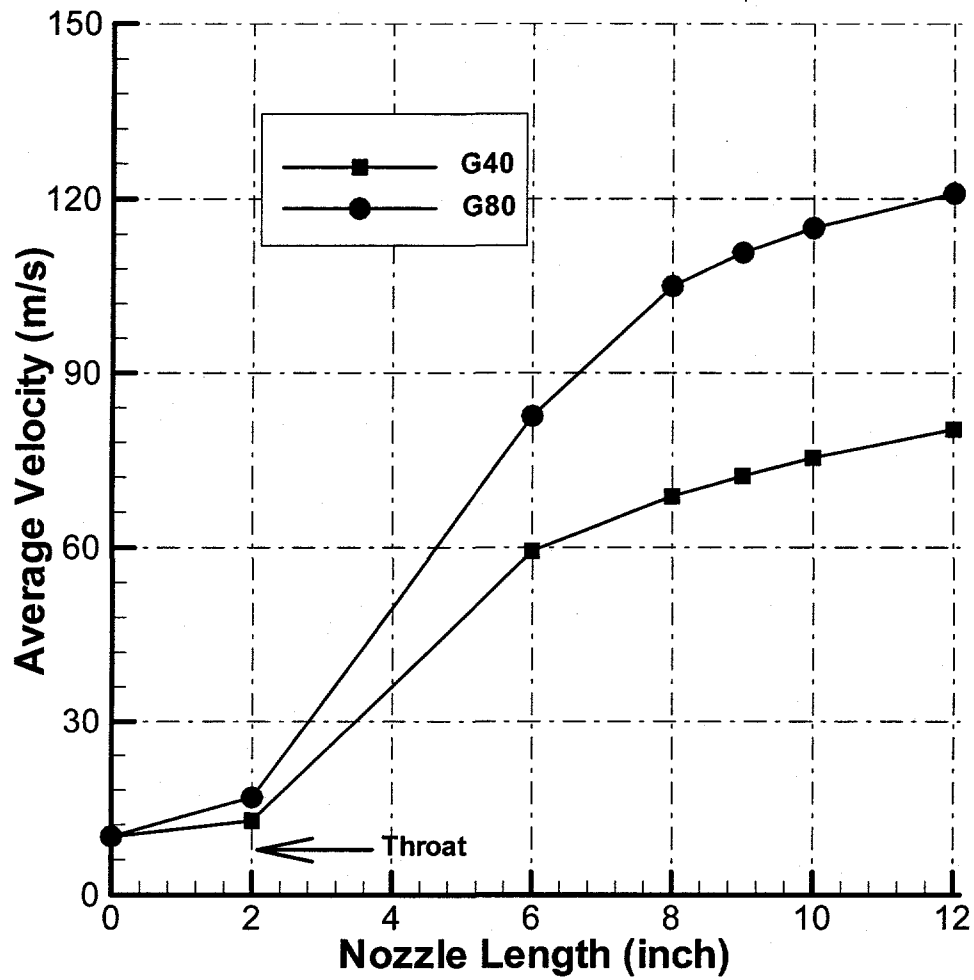


Figure 4. Particle velocities on the exit plane of the rectangular nozzle (1/4" equivalent throat diameter).

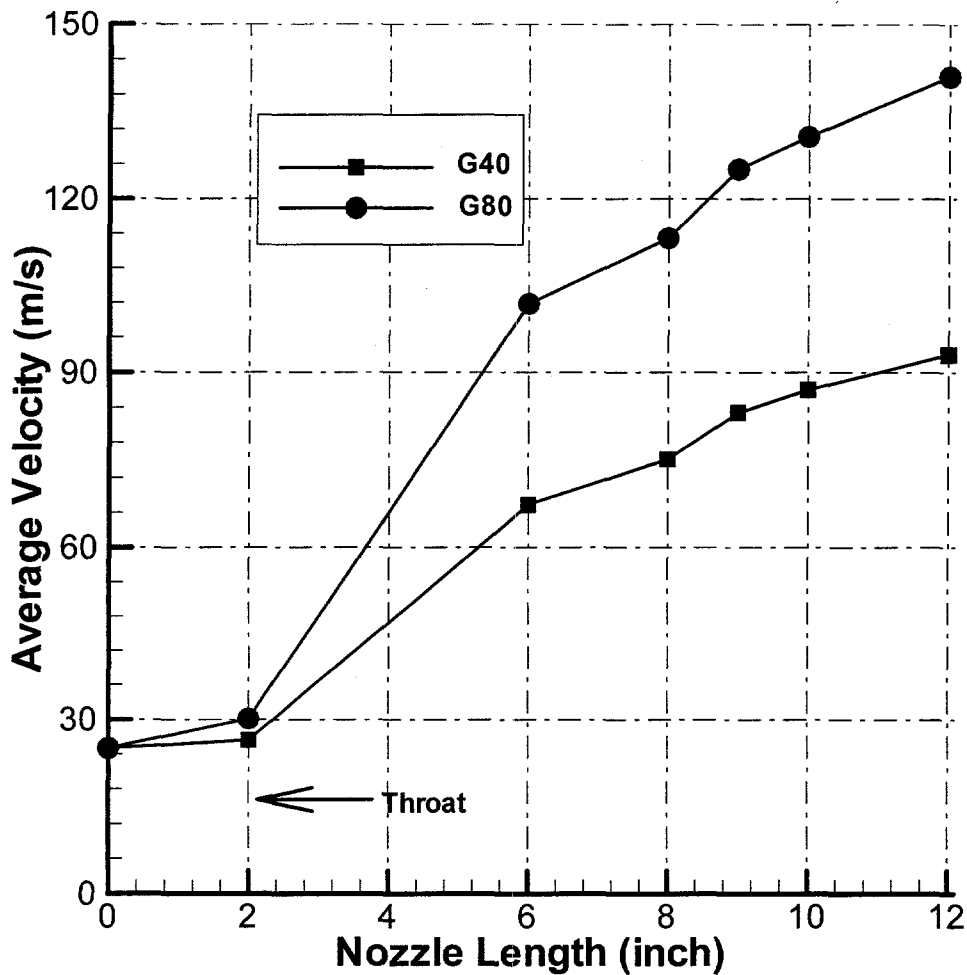


Figure 5. Particle velocities on the exit plane of the rectangular nozzle (3/8 inch equivalent throat diameter).

Based on the above numerical results and from the practical application point of view, the optimal geometry parameters of the rectangular nozzle were determined. Four rectangular nozzles with  $\frac{1}{4}$  and  $\frac{3}{8}$  inch equivalent throat diameter, and each with a different flow passage thickness, were chosen for further research.

### 1.2.3 Rectangular nozzle with $\frac{1}{4}$ inch equivalent throat diameter

With  $\frac{1}{4}$ -inch equivalent diameter, two nozzles with a  $\frac{1}{8}$  inch and a  $\frac{3}{16}$  inch flow passage thickness were calculated.

## Nozzle #1

Dimensions:	Inlet cross plane	1 x 1 inch
	Throat cross plane	13/32 x 2/16 inch
	Outlet cross plane	23/16 x 2/16 inch
	Convergent length	2 inches
	Divergent length	6 inches
	Total Length	8 inches

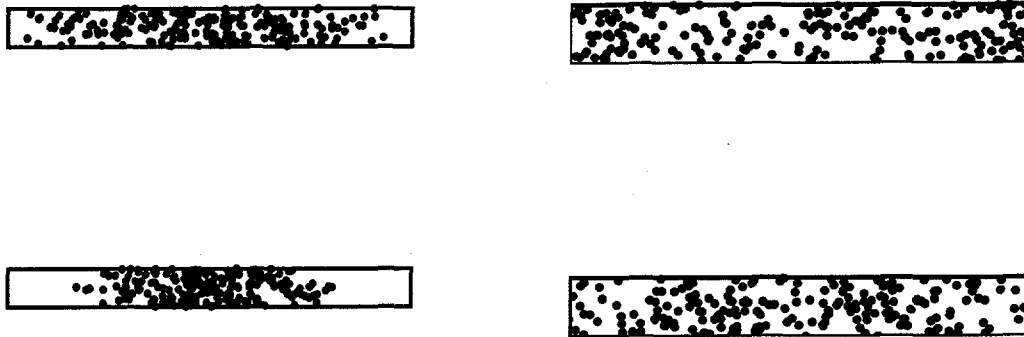
## Nozzle #2

Dimensions:	Inlet cross plane	1 x 1 inch
	Throat cross plane	17/64 x 3/16 inch
	Outlet cross plane	23/16 x 3/16 inch
	Convergent length	2 inches
	Divergent length	6 inches
	Total Length	8 inches

The difference between the above two nozzles exists in the flow passage thickness. One is 1/8 and the other is 3/16 inch, respectively. Table 1 illustrates the particle velocities for the two nozzles with grit G40 and G80. It seems that the thickness does not affect the particle velocity more, and the velocities with fine grit G80 are always higher than those with coarse grit G40. Compared with the numerical results of the existing round nozzle at the same conditions (45m/s for G40 and 70m/s for G80), the statistic average particle velocities at the exit plane of the nozzle are increased more than 50%. Figure 6 shows the particle distribution at the exit plane. It is better for the nozzle with 3/16 inch flow passage thickness. The particles nearly cover the whole cross-section of the exit plane.

**Table 1.**  
The average particle velocities at the exit plane of the rectangular nozzle

	Nozzle #1	Nozzle #2
Particle: G40	67 m/s	62 m/s
Particle: G80	104 m/s	100 m/s



(a) Nozzle #1, Top-G40, Bottom -G80

(b) Nozzle #2, Top-G40, Bottom -G80

**Figure 6. Particles distribution at exit plane of the nozzle.**

#### 1.2.4 Rectangular nozzle with 3/8-inch equivalent throat diameter

Similarly, two nozzles for 3/8 inch equivalent throat diameter, but with a 3/16 and a 4/16 inch flow passage thickness were calculated, and their flow passage dimensions are listed below:

##### Number #3

Dimensions:	Inlet cross plane	1 x 1 inches
	Throat cross plane	19/32 x 3/16 inch
	Outlet cross plane	3 x 3/16 inch
	Convergent length	2 inches
	Divergent length	6 inches
	Total Length	8 inches

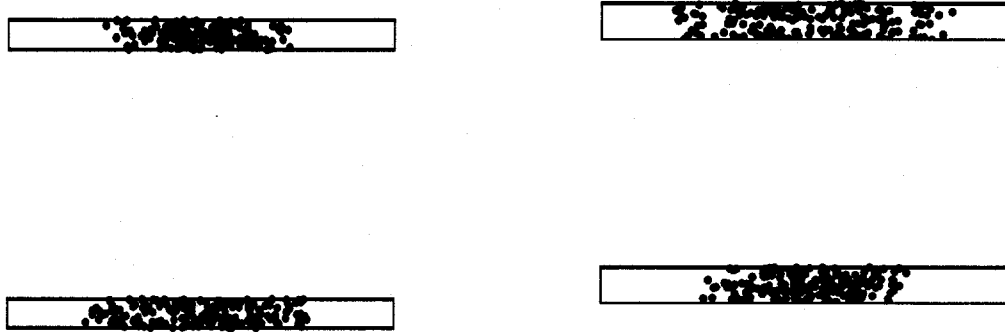
##### Number #4

Dimensions:	Inlet	1 x 1 inches
	Throat	14/32 x 1/4 inches
	Outlet	3 x 1/4 inches
	Convergent length	2 inches
	Divergent length	6 inches
	Total Length	8 inches

The only difference between the two nozzles above is the flow passage thickness. One is 3/16 inch, and the other is 4/16 inch. The flow passage thickness does not affect the particle velocity. It is estimated that a velocity of more than 100 m/s is expected with the fine grit G80. Table 2 shows the particle velocity, and Figure 7 gives the information on the particle distribution.

**Table 2.**  
**The average particle velocities at exit plane of the rectangular nozzle**

	Nozzle #3	Nozzle #4
Particle: G40	66 m/s	64 m/s
Particle: G80	103 m/s	100 m/s



(a) Nozzle #3, Top-G40, Bottom -G80

(b) Nozzle #4, Top-G40, Bottom -G80

**Figure 7. Particle distribution at exit plane of the nozzle.**

All of the above results were obtained at the ideal boundary condition: the inlet pressure was fixed at 100 psi, the wall of the nozzle was smooth, and the particles were considered as spherical, etc.

### 1.3 Numerical results and discussion (dust separators)

#### 1.3.1 Numerical results of the existing separator

In order to determine the performance of the existing separator, numerical simulations have been carried out. The geometry and air flow field of the existing separator is illustrated in Figure 8. In this case, the inlet boundary conditions were set at 10m/s for the average air velocity. Two-dimensional calculation was performed with incompressible flow assumption. Non-uniform, unstructured grids were chosen, and almost 20,000 elements were used to discretize the computation domain. Results show that the air flow is concentrated in the center of the cylinders. This pattern reflects the influence of the inserted inclined plates. Therefore, the result is reasonable based on the fluid mechanics. It is estimated that the relative concentrated air flow may bring some particles out of the separator during the separating process. The calculated results of the separation efficiency can prove the above conclusion. Under this condition, the

separation efficiency is about 90% for steel grit G40, but it is just about 27% for steel grit G80. Therefore, the centrifugal separator that replaces the existing one is needed when using finer steel grit.

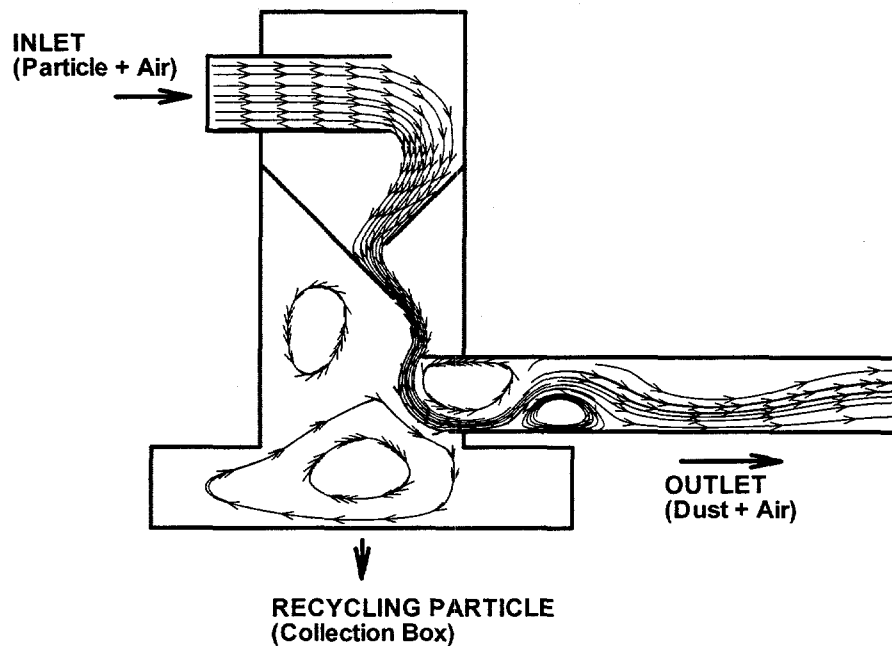


Figure 8. The geometry and air flow field of the existing separator.

### 1.3.2 Numerical results of the new centrifugal separator

Numerical modeling was performed to investigate the air flow field, particle trajectory, and collection efficiency. The inlet boundary condition is set to 10 m/s for the average air velocity. Fully three-dimensional calculations are performed with incompressible flow assumption. Non-uniform, unstructured grids are chosen to discretize the entire computation domain.

The geometry and grid system of the new centrifugal separator is shown in Figure 9, and almost 100,000 cells are used to discretize the computation domain. Figure 10 shows the air flow field in two symmetrical planes ( $x=0$ ) and ( $y=0$ ). The air flows down first, then turns to the exit of the separator due to the vacuum force. It is estimated that this air flow can entrain some small-sized particles out of the separator. Some large particles or heavy particles are collected in the bottom of the separator.

Figure 11 shows the influence of a separator's geometry on separation efficiency. First, with the increase of separator outside diameter, the separation efficiency increases. When the efficiency reaches the maximum value, it decreases with the outside diameter. Finally, the outside diameter that can provide the best separation efficiency is chosen for the new separator's outside diameter, i.e., 6 inches.



In this case ( the outside diameter is 6 inches), the calculated separation efficiency is about 70% for steel grit G80. Compared with the existing separator, the separator efficiency for steel grit G80 was almost double. Therefore, the new centrifugal separator can separate the finer grit well; of course, it can separate the coarse grit. The numerical results of efficiency for two types of separator are listed on Table 3.

**Table 3.**  
**Comparison of the efficiency of two separators**

	Existing separator	New centrifugal separator
Efficiency (steel grit G40)	90%	
Efficiency (steel grit G80)	27%	70%

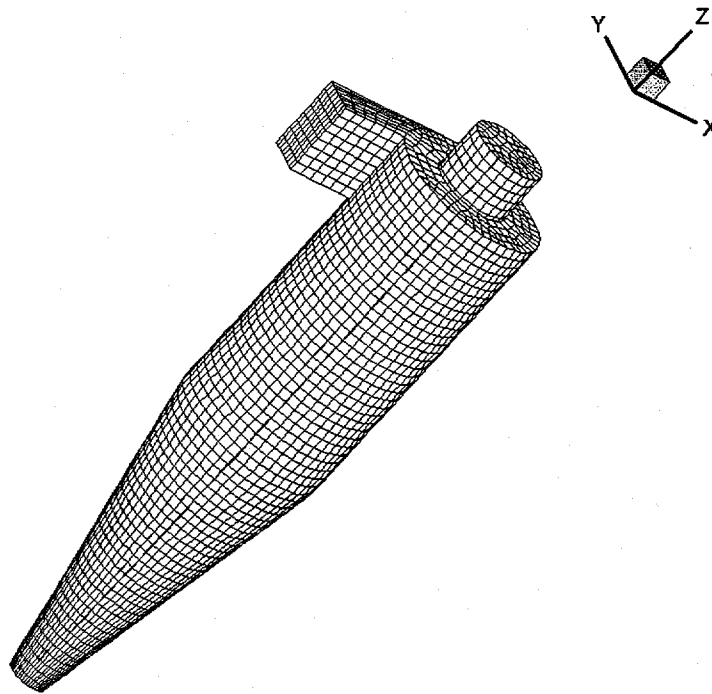


**Figure 9. The grid system of the new centrifugal separator.**

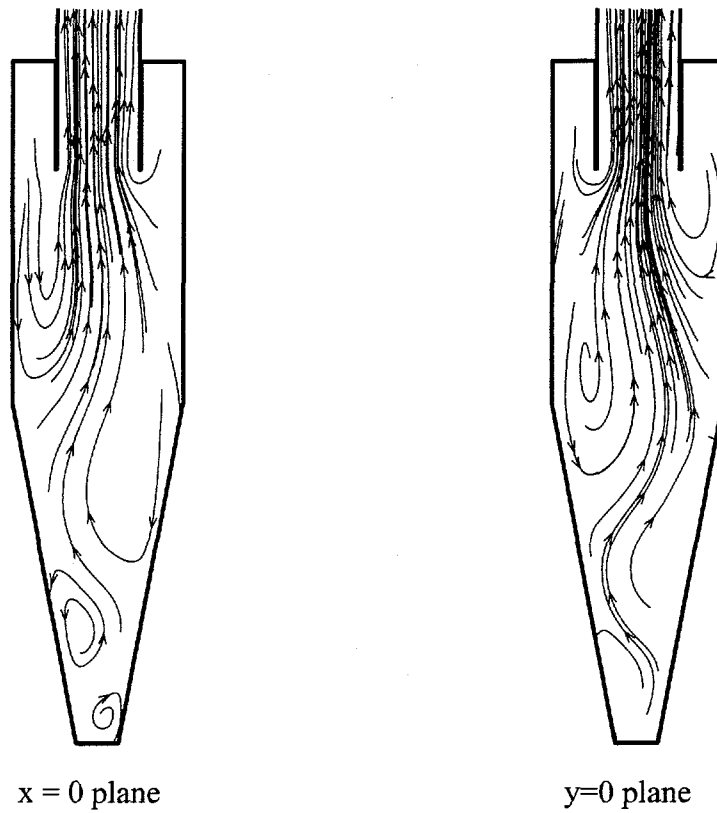


Figure 10. Air flow field on two symmetrical planes of the centrifugal separator.

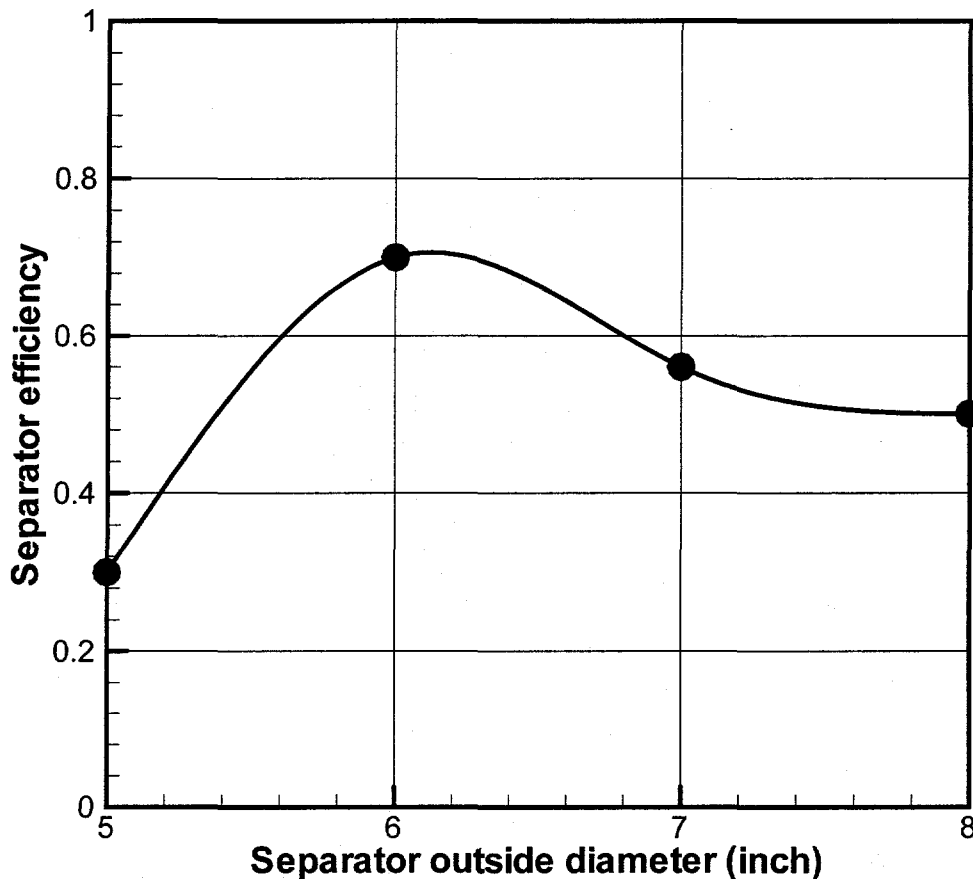


Figure 11. Outside diameter versus efficiency of centrifugal separator.

#### 1.4 Numerical results and discussion (wind curtain)

The wind curtain is expected to have two functions. One is to create an air barrier to prevent the particles escaping to the atmosphere. The other is to make the blasthead float on the wall surface and balance the forces. To achieve the above goals, a draft proposal is presented that is expressed in Figure 12.

Because the wall surface can not be very smooth, a gap between the wall surface and the blasthead was considered. The injected air has a fixed pressure, and the geometry has an inclined angle. The numerical modeling was performed to study the air flow field for the wind curtain. For the air injection system, the channel gap and the channel inclined angle are the main parameters. They are important parameters to affect the force balance within the whole system. The numerical modeling has been performed to obtain the optimal gap and the incline channel angle. The blasthead working distance is also an important parameter.

Three channel gaps of the wind curtain, of 1/16, 1/8 inch, and 1mm, were chosen for numerical modeling. The CFD modeling was conducted for each channel gap with 30°, 45°, and 60°

inclination angles. The assumed working distances are from 0.1 to 3 inch. In these calculations, the injection pressures are fixed to be 1.2 ~ 3.0 bar and the vacuum pressure is set as 0.2 bar. One of the calculation cases on the air flow field in the wind curtain is shown in Figure 13. The assumed working distance effect on wind curtain efficiency, which means the statistical percentage of particles contained inside the wind curtain, at different inject pressure is shown on Figure 14. With an increase of injection pressure, the wind curtain efficiency can increase to almost 100% at some specific working distances. Therefore, the proposed wind curtain will be able to meet the desired need.

The lift force can also be balanced. The criteria of the optimum parameters are based on calculated results and a practical view. Under the conditions that the injection pressure is below 1.5 bar, the vacuum pressure is above 0.2 bar, and more than 95% of G80 grit will be contained inside the wind curtain, the calculated results provide the following optimal parameters: the channel gap is 1mm to 2mm; the incline angle is 45° to 60°; the working distance is less than 1 inch.

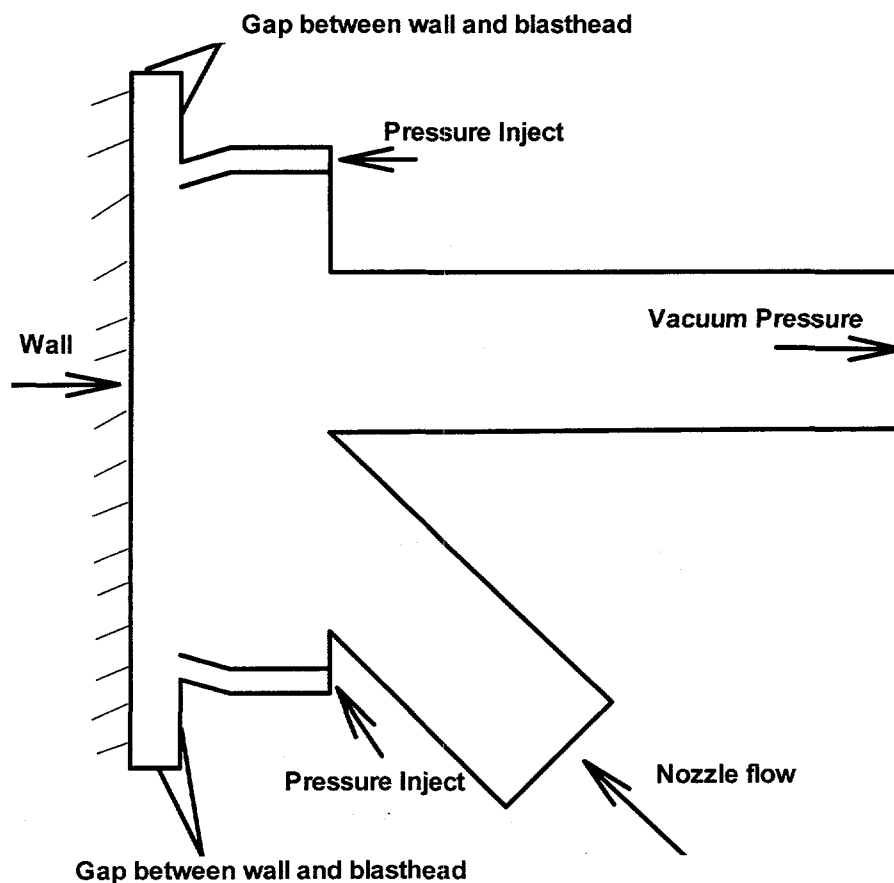
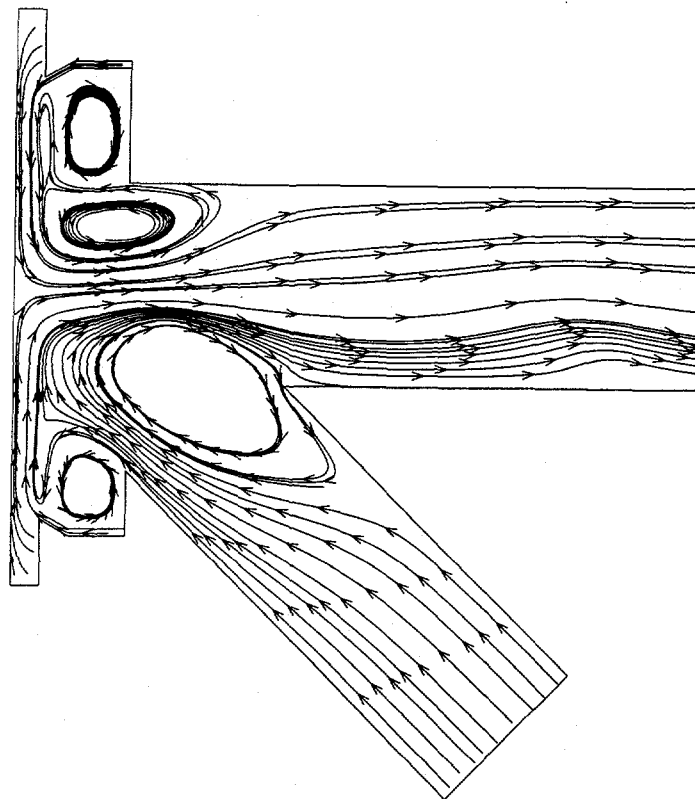


Figure 12. Proposed geometry of wind curtain.



**Figure 13. Air flow field on the proposed wind curtain (gap=1/16 inch, angle = 60°, working distance = 0.25 inch).**

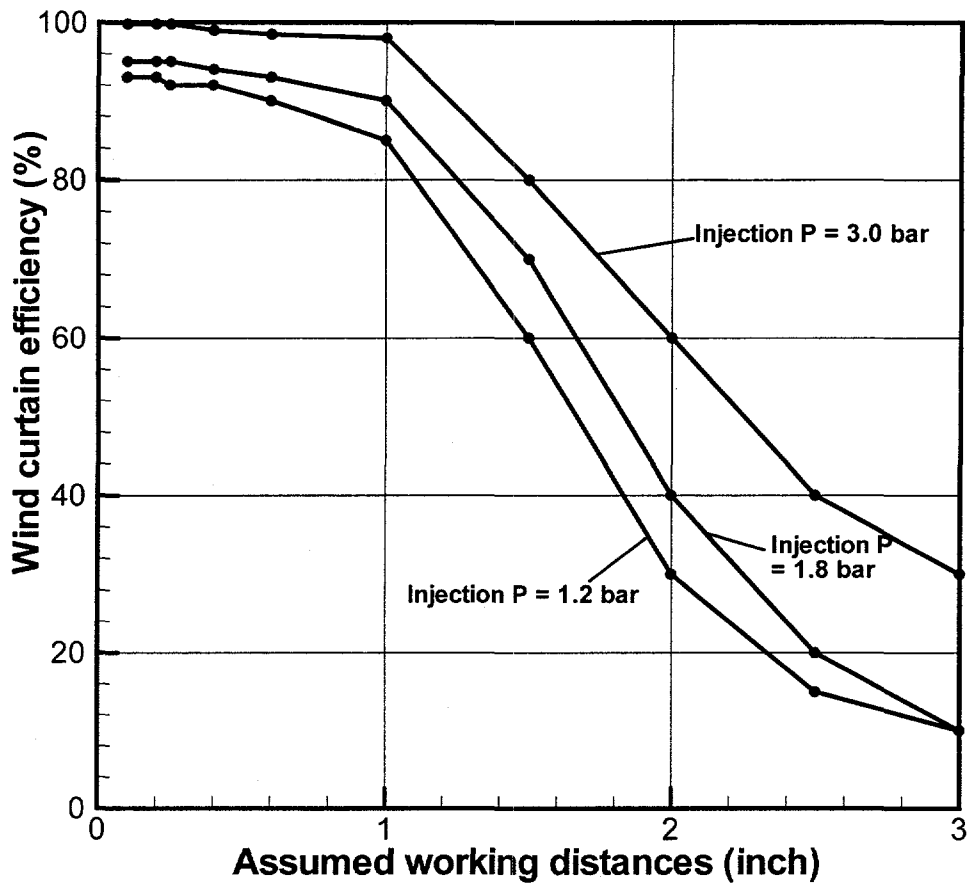


Figure 14. Assumed working distance versus the wind curtain efficiency at different injection pressure.

## PART 2. NEW DESIGN FOR RECTANGULAR NOZZLE, CENTRIFUGAL SEPARATOR, BLASTHEAD/ WIND CURTAIN, AND BLASTHEAD SENSOR

---

### 2.1 The design of the new rectangular nozzle

Based on the numerical simulation data, three nozzle types have been designed. Two nozzles are for the equivalent throat diameter of  $\frac{1}{4}$  inch with  $\frac{1}{8}$  and  $\frac{3}{16}$  inch flow passage thickness. The third nozzle type is for the equivalent throat diameter of  $\frac{3}{8}$  inch. In phase 1, only one nozzle with the throat equivalent diameter of  $\frac{1}{4}$  inch was tested. Table 4 lists the geometry of the newly designed nozzle, which is shown in Figure 15. The detailed design drawings of the rectangular nozzle are presented in Appendix A.

**Table 4.**  
**Flow passage dimensions of the rectangular nozzle ( $\frac{1}{4}$ - inch equivalent diameter)**  
**(Compared with the existing round nozzle)**

	Round nozzle	Rectangular Nozzle
Description	Dimensions, inches	Dimensions, inches
a, length of the divergent section	2.18	6
b, length of the convergent section	1.68	2
c, width of the inlet cross-section	$\phi 0.97$ (inlet diameter)	1
d, thickness of the inlet cross-section	$\phi 0.97$ (inlet diameter)	1
e, thickness of the nozzle	$\phi 0.25$ (throat diameter)	$\frac{1}{8}$
f, width of the exit plane	$\phi 0.722$ (outlet diameter)	$\frac{23}{16}$

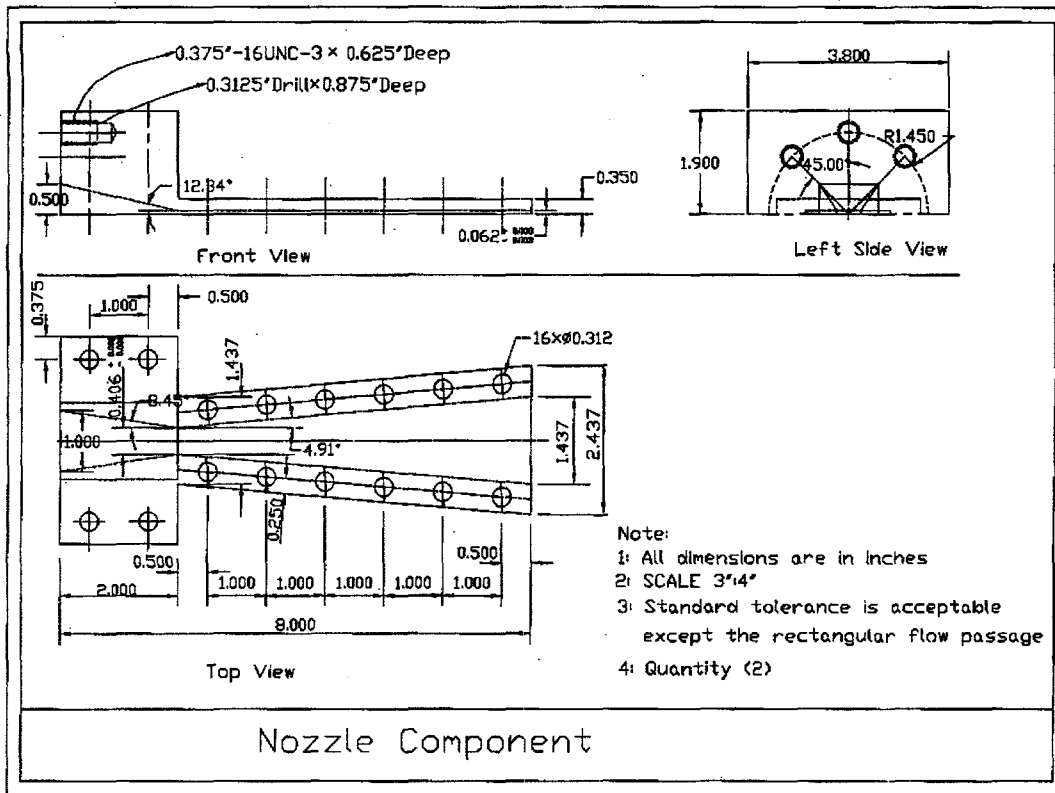


Figure 15. AutoCAD drawing of the newly designed nozzle.

## 2.2 The design of new centrifugal separator

Similarly, based on the modeling data, a new centrifugal separator has been designed and manufactured. The detailed AutoCAD drawing is shown in Figure 16. In the figure, numbers 1 ~ 9 are the detail drawings for each part, which are shown in Appendix B.



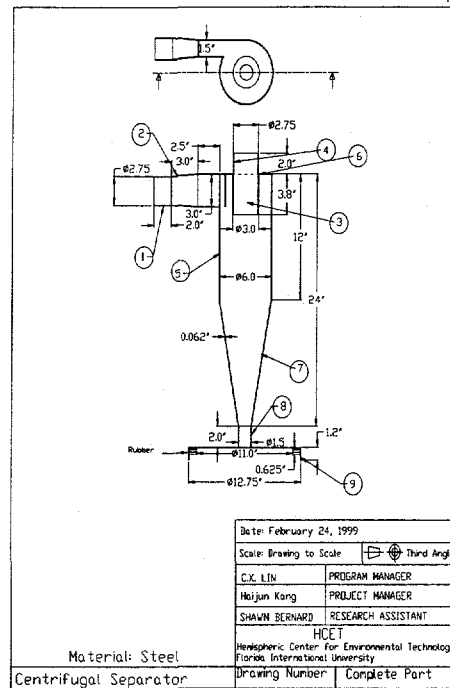


Figure 16. Newly designed centrifugal separator.

### 2.3 The design of the new blasthead/wind curtain with $\frac{1}{4}$ inch equivalent diameter nozzle

The blasthead/wind curtain has been designed with the analysis of numerical simulation results. Figure 17 illustrates the blasthead with 0.25 inch equivalent diameter, made up of eight components. The air-steel two-phase flow jet with high velocity strikes the ground surface to be cleaned at a  $45^\circ$  angle. The present design makes the air-steel jet arrive at the surface nearly from the center of the blasthead. This arrangement makes the dust suction up the vacuum pipe easily. The vacuum pipe is used to suck the dust mixture. The wind curtain is a circular convergent-parallel nozzle, with  $15^\circ$  relative to the vertical coordinate in the convergent section and  $45^\circ$  relative to the vertical coordinate in the parallel section. The design can achieve sonic velocity at the outlet of the nozzle, and the air barrier has enough hardness. In other words, the hard thin air film can be formed to keep the steel/dust mixture from escaping to the outside environment. The circular gap between the inside part and the outside part of the wind curtain is taken as 1.0 mm. The detailed drawings of every component are presented in Appendix C.

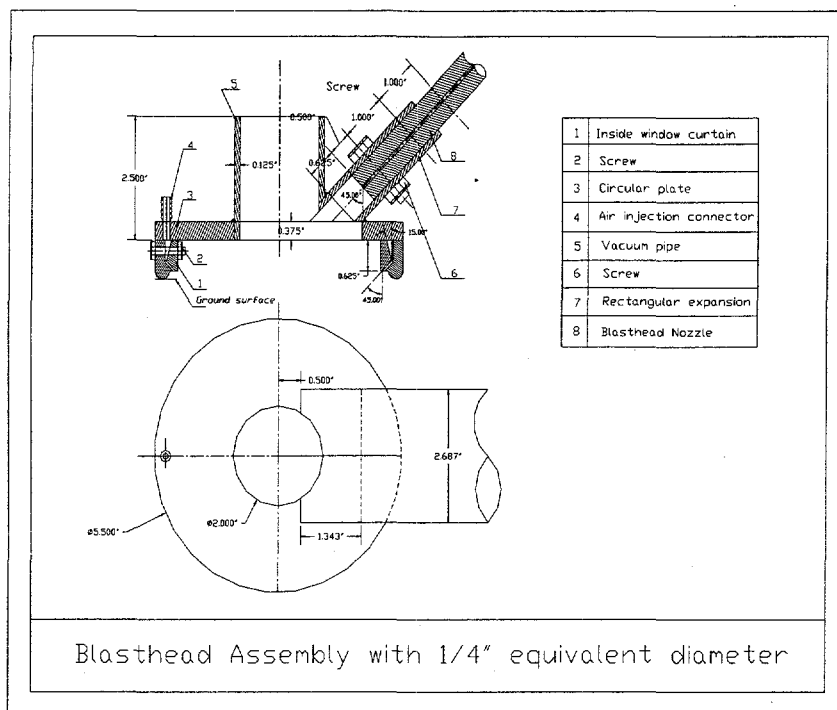


Figure 17. Newly designed blasthead with 0.25 inch equivalent diameter.

## 2.4 Blasthead sensors

### 2.4.1 Radiological characterization sensor system

The concept design is complete. The system will have four major subsystems: transducers (2); transducer interface electronic modules (2); control electronic module; and operator interface module; see Figure 18.

The transducers (2) will be incorporated into the structure of the blasthead as compactly as possible to minimize the standoff distance from an adjacent perpendicular surface, Figures 19 and 20. A transducer is situated in the forward path, and a second transducer is situated in the following path of the blasthead. This arrangement allows feedback to the operator indicating degree of contamination and success at decontamination. Transducers used in a given application can be any of the commonly used cylindrically shaped radiation sensors such as Geiger-Mueller, gas proportional, or scintillator/photosensor, as shown in Figure 21. The initial demonstration prototype will contain end-window Geiger-Mueller tubes of an industry/government standard specification. Sensitivity is nominally 4300 cpm at 1 mR/hr Cs137. The tube diameter is 16mm (0.63 in.), and a collimating/background shield of 5 mm (0.19 in.) thickness lead (tungsten optional) will surround the tube. Total weight of each assembly is approximately 700g (1.5 lb.). Most of the weight of this assembly is contributed by the heavy metal shield. Alternative transducers of reduced sensitive height, of limited susceptibility to background, or lower penetrability background will significantly reduce the weight.

The transducer interface modules will be commercial packed modules incorporating regulated HV power supply, electrometer amplifier, pulse height discriminator and shaper, rate meter, and digital serial interface. One module is associated with each transducer. The modules are programmable to provide an interface to the full range of anticipated transducer types. Each module is approximately 11.2 x 6.2 x 2.6 cm (4.4 x 2.4 x 1 in) and weighs 200g (7 oz.). Following confirmation of the prototype, advanced design for transfer to production will allow consolidation of interface electronics within the control/operator module with a significant attendant reduction in size and weight.

The control electronics module is a custom design incorporating industry standard microcontroller components. The module will interface with the two transducer interface modules and the operator interface to compensate for background (establish offset), to set the acceptance level (establish range), and to convert the signal for display. Pseudocode has been written based on logic flowcharts, and the final code will be written using an accepted compilation mechanism to assure maintainability. The control electronics module will be contained within the package housing the operator interface module.

The operator interface module incorporates two circular digital high intensity LED bargraphs for sensed contamination level feedback. In addition, push buttons enabling collective background level setting and individual span calibration are included along with digital thumbwheel switches to set allowable span settings to previously determined engineering units if desired as an alternative to direct calibration from sources, Figure 22. The initial prototype assembly of operator interface and control electronics will have a size and weight anticipated as 20 x 12 x 12 cm (8 x 5 x 5 in.), 450g (1 lb.). This package is excessive in size and weight and is dictated by the expediency of using off-the-shelf components for display. A refined design with appropriately sized displays will follow in phase 2 with a size approaching 12 x 7 x 7 cm (5 x 3 x 3 in.) and 300 g (12 oz.).

A simplified operation and control scenario has been generated that minimizes the requirement of the operator to be knowledgeable in characterization. The intent is to provide a system that effectively allows the operator to visualize the removal of an invisible contaminant. A potential extension of this concept is substitution of non-radiological transducers into the blasthead for detection of other contaminants, such as heavy metals or organic chemicals.

#### *2.4.2 Lift-off sensor system*

Two conceptual lift-off sensor system designs have been generated. The preferred design incorporates sensitive differential pressure switches/transducers to monitor the generated negative pressure within the blasthead. Any significant separation of the head from the surface will necessarily reduce the effective vacuum. An anticipated additional beneficial effect is an incipient failure of the vacuum effluent retrieval system and will be detected. This concept is most efficient in use of space and weight, as well as superior in expected effectiveness.

The alternative design incorporates non-contact distance measuring switches/transducers arranged in a triangular pattern within the periphery of the blasthead. This method is fundamentally more expensive in terms of size, weight, and cost than the preferred technique. The switches/transducers can be optical or capacitive in technology; both will be analyzed. While the deficits of this design are understood, preliminary design is proceeding as an alternative.

Lessons learned from previous relatively crude attempts to monitor blasthead pressure indicate that external factors can complicate the implementation of a system based on such a technique. Direct measurement of the separation of the blasthead from the surface also has endemic difficulties, and application of the measurement to an indication of functional lift-off is not necessarily trivial. Lift-off sensor final design is awaiting an operational blasthead with air curtain to allowing testing of concepts.

Control and indication of the lift-off sensor system will be contained within the characterization system modules. A control signal will be provided to power a pinch valve or other mechanism to inhibit the flow of abrasive during a sensed lift-off condition. Size and weight of the system will depend upon the chosen technique and the final configuration of the blasthead.

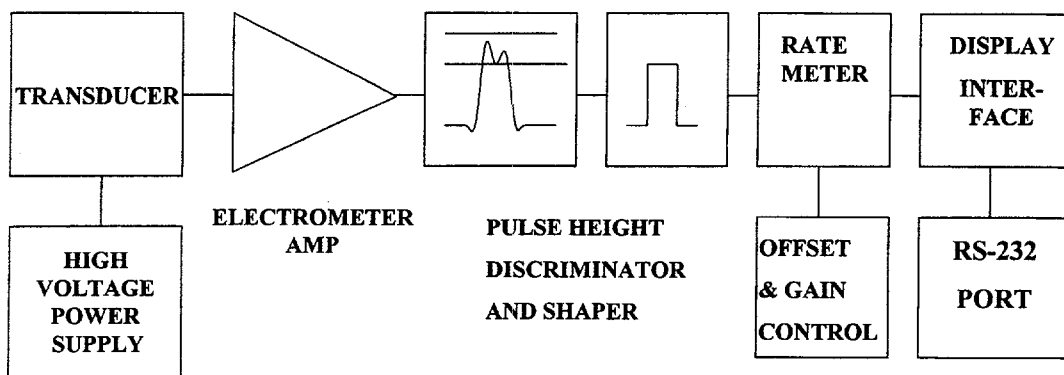


Figure 18. Radiological characterization electronics.

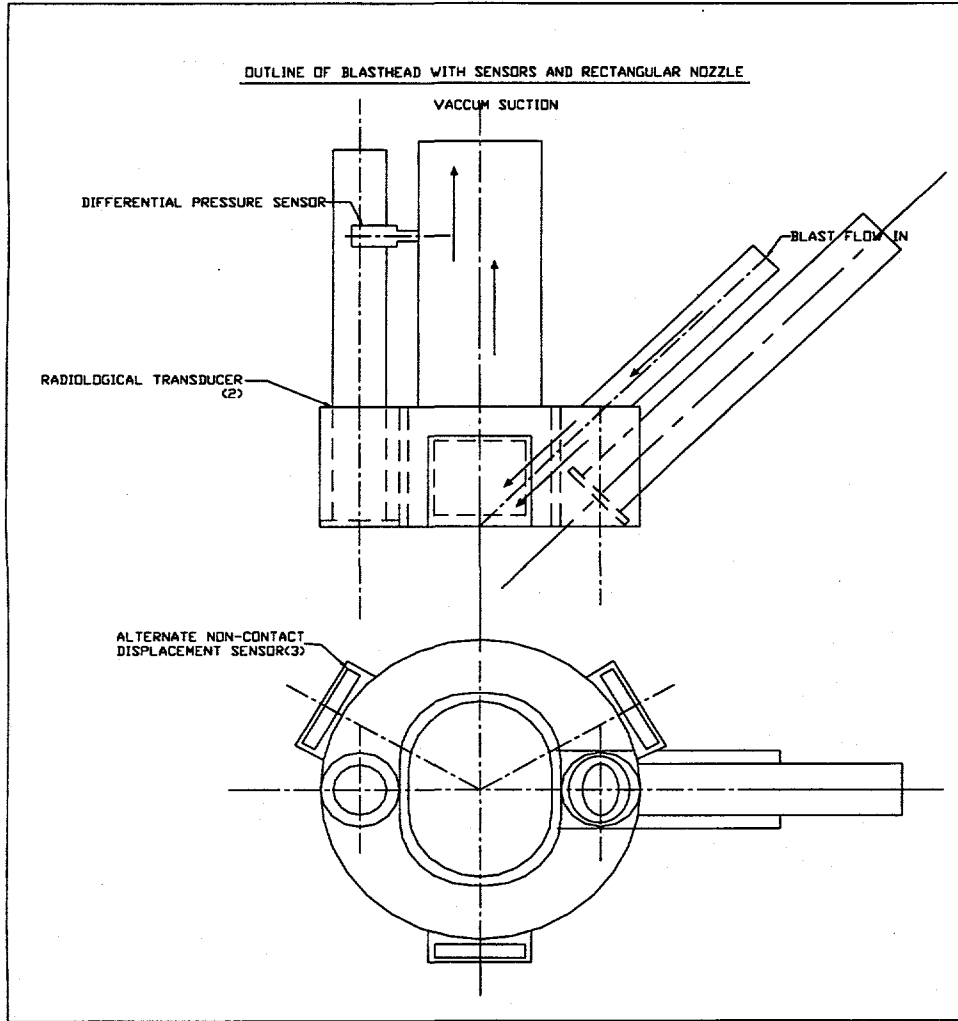
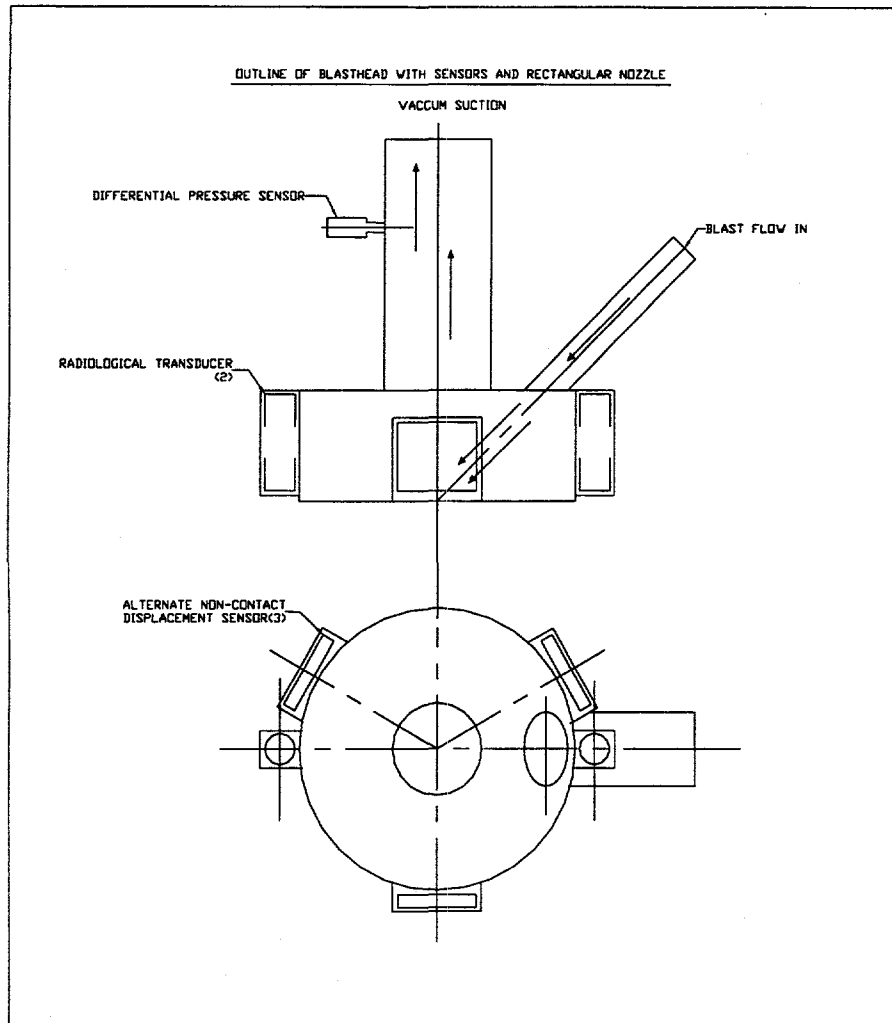


Figure 19. Possible arrangement of sensor component with compact blasthead chamber design.



**Figure 20. Possible arrangement of sensor components with large blasting chamber design.**

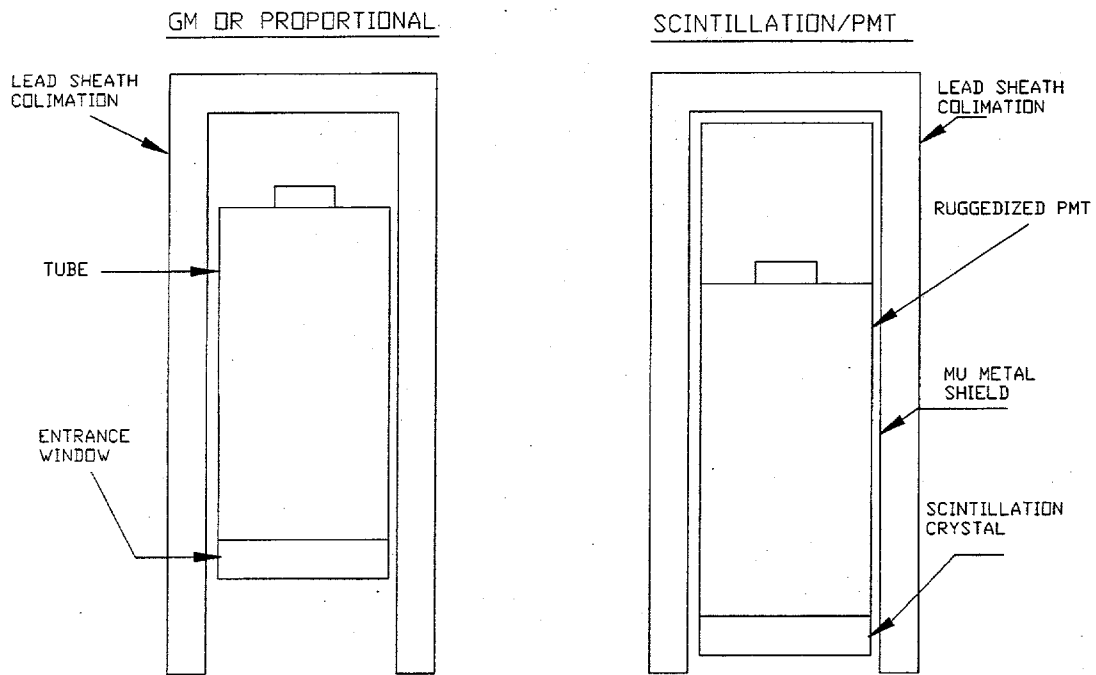


Figure 21. Radiological transducer assemblies.

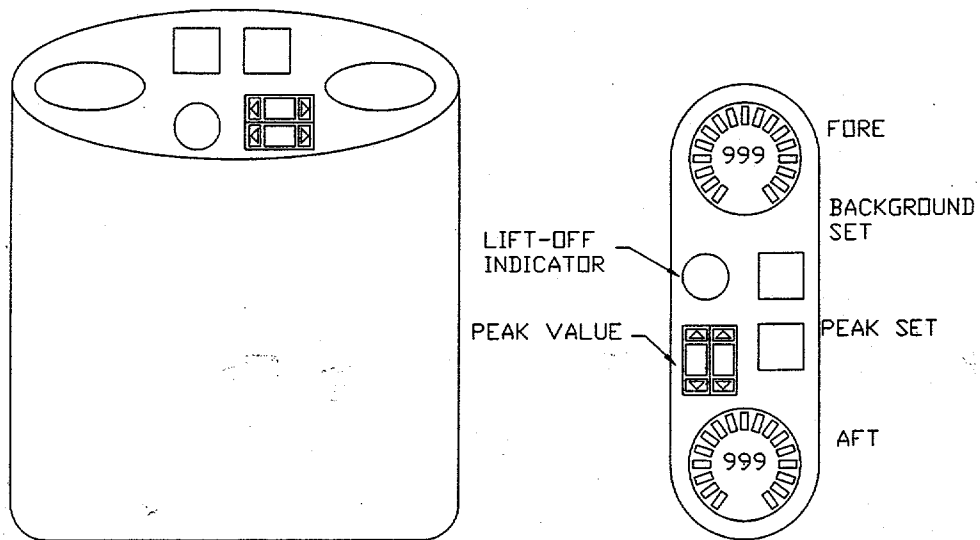


Figure 22. Electronic/indicator POD.

## **PART 3. MODEL TEST**

---

The objective of this report is to present the experimental results on the blasting nozzle and the new centrifugal separator, as well as the comparisons with CFD modeling. A flow loop, with air-particle two-phase flow has been set up. Combined with the LTC Vacuum Blasting Machine, the facilities have been successfully running. With the Phantom High-Speed Video Camera system, the particle velocity and their concentrations are measured, for both the existing circular nozzle and the new rectangular nozzle of ¼ inch diameter. The measurements matched the CFD modeling well, with the maximum distinction below 10.0%. A 6060P Pitot probe from ALNOR INSTRUMENT COMPANY was employed to obtain the velocity distribution. The comparison of experimental data and CFD modeling results showed that the design of the new centrifugal separator was successful.

### **3.1. Experimental results and their comparison with CFD modeling on the blasting nozzle**

#### *3.1.1 Description of setup*

Figure 23 illustrates the layout of the experimental setup. The LTC Vacuum Blasting Machine has been used to produce the blasting air-particle two-phase flow and the vacuum pipeline will be used to recycle the steel grit. As shown in Figure 23, the air compressor generates the high-pressure air. The high-pressure air is divided into three pipelines. Pipeline 1 is connected to the vacuum generator to produce vacuum. Pipeline 2 is connected to the pressure vessel. The air flow from pipeline 2 controls the valves (inside the pressure vessel) so that the steel grit can be drained from the upper chamber to the lower chamber in the pressure vessel. Of the three pipelines, pipeline 3 is the most important one. This pipeline produces the air-particle two-phase flow when the air is mixed with the steel grit that is drained from the lower chamber of the pressure vessel (see Figure 23). The air flow rate and the temperature are measured before the air is mixed with the grits.

#### *3.1.2 Working mechanism*

The air-particle two-phase mixture flows through the blasting nozzle. At the exit of the nozzle, the steel grit particles have a higher velocity. Between the blasting nozzle and the collection box, there is a rectangular glass channel (1×1 ft) with a length of 2 ft, through which the steel particles pass as a high-speed jet. The collection box collects the steel grit from the nozzle. This collection box is connected with the vacuum pipeline that is used to recycle the grit, after transporting the grit particles in the machine (see Figure 23).

#### *3.1.3 Instruments*

Three instruments are installed in pipeline 3 to measure the air flow rate, air temperature, and air pressure, as illustrated in Figure 23. The Phantom v3.0 High Speed Digitor Motion Analysis System is used to measure the steel grit velocity and the steel grit concentration in the experimental setup. The complete Phantom system includes three major components: a high-speed camera, pulsed laser source, and PIV software. This system is the combination of a high-



speed imager, capturing several thousand images per second, with the short duration sheet lighting formed by pulsed laser, that allows us to create sharp, clear pictures of a cross-sectional area of the flow. Since the pulsed duration of the laser (and hence the exposure time per image) is only 30 nanoseconds, the pictures will be sharp and blur-free to facilitate the measurements. After an image is complete, the PIV software is used to do particle tracking, auto or cross-correlation.

Figure 24 illustrates the measurement mechanism of the particle velocity and concentration. The nozzle produces the high speed air-particle jet along the x coordinate. Y is the vertical coordinate. The pulsed laser creates a vertical laser sheet with very short time duration and separation. Because the environment is "dark," the moving particles can only be captured when the laser is on. The first dot is created on the image when the first laser pulse arrives. Continuously the second dot will be produced when the second laser pulse comes. The time difference between the first and the second laser pulse is defined as the time separation. For the present measurement, the particle velocity is very high; thus, short time separation is needed. The experiments show that it is suitable to choose the time separation of 25  $\mu$ s. Four laser pulses create four dots in the image, and the total time is  $3 \times 25 \mu$ s. The following simple expression is used to calculate the particle velocity:

$$v = \frac{d \times 10^{-3}}{3 \times 25 \times 10^{-6}}$$

The units of d and v are mm and m/s, respectively.

Next is particle concentration measurement. Through data processing of the image file, two lines, lines AB and CD, can be identified to cover all particle dots in the image. Extending the two lines to the nozzle exit plane obtains the line EF, which is identified as the length of the particle coverage in y direction. For the circular nozzle, EF is the circular diameter that the particles cover at the nozzle exit plane. For the rectangular nozzle, two measurements are conducted: one with long side (EF) at horizontal position, and the other with long side (EF) at vertical position. Through data processing, the covering area of the particles at the exit plane can also be obtained.

Figure 25 shows the measurement arrangement for the existing circular nozzle with 1/4 inch throat diameter. Only one arrangement is needed due to the symmetry. Figure 26 and Figure 27 show the two measurement arrangements for the new rectangular nozzle, which were mentioned above. For the present application, the duration and the separation are chosen to be 5  $\mu$ s and 25  $\mu$ s. The main part of the practical experiment setup for the blasting nozzle test is shown in Figure 28.

#### 3.1.4 Test section

Two test sections were used. One is the existing round nozzle, and the other is the new rectangular nozzle. Their detailed dimensions were described in Table 4. For the circular nozzle, the length of the convergent section is 1.68 inches, and the divergent section possess the length of 2.18 inches.

The new rectangular nozzle has the gap of 1/8 inch. The lengths of the convergent section and the divergent section are 2 and 6 inches, respectively. The equivalent diameter at the throat

location is ¼ inch. Compared with the classical circular nozzle, the new rectangular nozzle is a longer nozzle.

### 3.1.5 Experimental results and comparison with CFD modeling

Excellent image files were acquired, and the test cases are listed in Table 5.

**Table 5.**  
**Six test cases**

Nozzle	Test Pressure, Psi	Nozzle Arrangement
Circular Nozzle	65	See Fig.25
Circular Nozzle	83	See Fig.25
Rectangular Nozzle	65	With long side at horizontal position, see Fig.26
Rectangular Nozzle	82	With long side at horizontal position, see Fig.26
Rectangular Nozzle	65	With long side at vertical position, see Fig.27
Rectangular Nozzle	82	With long side at vertical position, see Fig.27

Table 6 and Table 7 provide the typical data points for the existing round at inlet pressure of 83 psi and 65 psi. Table 8 and Table 9 are for the rectangular nozzle with long side at horizontal position at inlet pressure of 82 Psi and 65 Psi, respectively.

**Table 6.**  
**Typical data points of grit velocity measurement**  
**(existing round nozzle, ¼ inch, pressure=83 psi)**

Data Point No.	Distance, mm	Time, $\mu$ s	Measured velocity, m/s
1	4.152	$3 \times 25 \mu$ s	55.4
2	4.948	$3 \times 25 \mu$ s	59.8
3	5.204	$3 \times 25 \mu$ s	69.4
4	4.598	$3 \times 25 \mu$ s	61.3
5	3.35	$3 \times 25 \mu$ s	44.7
6	4.146	$3 \times 25 \mu$ s	55.3
7	4.954	$3 \times 25 \mu$ s	66.1

Data Point No.	Distance, mm	Time, $\mu$ s	Measured velocity, m/s
8	5.538	$3 \times 25 \mu$ s	73.8
9	4.261	$3 \times 25 \mu$ s	56.8
10	4.263	$3 \times 25 \mu$ s	56.8
11	4.958	$3 \times 25 \mu$ s	66.1
12	3.572	$3 \times 25 \mu$ s	47.6
13	4.492	$3 \times 25 \mu$ s	59.9
14	3.463	$3 \times 25 \mu$ s	46.2
15	4.031	$3 \times 25 \mu$ s	53.7
16	4.378	$3 \times 25 \mu$ s	58.4
17	4.390	$3 \times 25 \mu$ s	58.5
18	4.038	$3 \times 25 \mu$ s	53.8
19	5.100	$3 \times 25 \mu$ s	68.0
20	4.268	$3 \times 25 \mu$ s	56.9
21	5.999	$3 \times 25 \mu$ s	80.0
22	4.843	$3 \times 25 \mu$ s	64.5
23	3.578	$3 \times 25 \mu$ s	47.7
24	3.923	$3 \times 25 \mu$ s	52.3
25	3.340	$3 \times 25 \mu$ s	44.5
26	4.370	$3 \times 25 \mu$ s	58.3
27	4.489	$3 \times 25 \mu$ s	59.8
28	4.265	$3 \times 25 \mu$ s	56.7
			Average velocity=58.3

**Table 7.**  
**Typical data points of grit velocity measurement**  
**(existing round nozzle, ¼ inch, pressure=65 psi)**

Data Point No.	Distance, mm	Time, $\mu$ s	Velocity, m/s
1	3.35	3 $\times$ 25	44.6
2	3.58	3 $\times$ 25	47.7
3	3.42	3 $\times$ 25	45.6
4	4.12	3 $\times$ 25	54.9
5	4.04	3 $\times$ 25	53.9
6	3.92	3 $\times$ 25	52.3
7	3.12	2 $\times$ 25	41.6
8	4.38	3 $\times$ 25	58.4
9	3.46	3 $\times$ 25	46.1
10	3.20	3 $\times$ 25	42.7
11	3.56	3 $\times$ 25	47.5
12	3.80	3 $\times$ 25	50.7
13	4.04	3 $\times$ 25	53.9
14	4.10	3 $\times$ 25	54.7
15	4.02	3 $\times$ 25	53.6
16	3.96	3 $\times$ 25	52.8
17	3.84	3 $\times$ 25	51.2
18	3.22	3 $\times$ 25	42.9
19	3.28	3 $\times$ 25	43.7
20	3.24	3 $\times$ 25	43.2
21	3.48	3 $\times$ 25	46.4
22	3.32	3 $\times$ 25	44.3
23	3.38	3 $\times$ 25	45.1
24	3.52	3 $\times$ 25	46.9
25	3.40	3 $\times$ 25	45.3
26	3.28	3 $\times$ 25	43.7
27	3.26	3 $\times$ 25	43.5
28	3.62	3 $\times$ 25	48.3
			Average velocity=48.8

**Table 8.**  
**Typical data points of grit velocity measurement**  
**(the new rectangular nozzle, ¼ inch equivalent diameter, pressure=82 psi)**

Data Point No.	Distance, mm	Time, $\mu$ s	Velocity, m/s
1	8.35	3 $\times$ 25	111.3
2	10.2	3 $\times$ 25	136.0
3	7.55	2 $\times$ 25	100.7
4	8.50	3 $\times$ 25	113.3
5	8.92	3 $\times$ 25	118.6
6	9.80	3 $\times$ 25	130.6
7	7.22	3 $\times$ 25	96.0
8	8.24	3 $\times$ 25	109.3
9	8.52	3 $\times$ 25	113.3
10	8.20	3 $\times$ 25	109.0
11	8.50	3 $\times$ 25	113.3
12	7.88	3 $\times$ 25	105.1
13	7.64	3 $\times$ 25	101.9
14	9.84	3 $\times$ 25	131.2
15	9.10	3 $\times$ 25	121.3
16	8.14	3 $\times$ 25	108.5
17	8.12	3 $\times$ 25	108.3
18	8.16	3 $\times$ 25	108.8
19	8.24	3 $\times$ 25	109.7
20	8.16	3 $\times$ 25	108.8
21	7.88	3 $\times$ 25	105.1
22	7.70	3 $\times$ 25	102.7
23	9.06	3 $\times$ 25	120.8
24	8.10	3 $\times$ 25	108.0
25	8.04	3 $\times$ 25	107.2
26	8.08	3 $\times$ 25	107.7
27	8.54	3 $\times$ 25	113.6
28	8.60	3 $\times$ 25	114.7
			Average velocity=112.0

**Table 9.**  
**Typical data points of grit velocity measurement**  
**(the new rectangular nozzle, ¼ inch equivalent diameter, pressure=65 psi)**

Data Point No.	Distance, mm	Time, $\mu$ s	Velocity, m/s
1	6.71	3 × 25	89.3
2	6.70	3 × 25	89.3
3	6.51	3 × 25	86.6
4	6.10	3 × 25	81.3
5	6.81	3 × 25	90.4
6	7.02	3 × 25	93.3
7	6.82	3 × 25	90.6
8	7.21	3 × 25	96.0
9	6.21	3 × 25	82.6
10	6.04	3 × 25	80.5
11	5.84	3 × 25	77.9
12	5.78	3 × 25	77.1
13	5.92	3 × 25	78.9
14	6.02	3 × 25	80.3
15	5.80	3 × 25	77.3
16	5.76	3 × 25	76.8
17	5.74	3 × 25	76.5
18	6.12	3 × 25	81.6
19	6.08	3 × 25	81.1
20	6.02	3 × 25	80.3
21	6.14	3 × 25	81.9
22	5.80	3 × 25	77.3
23	5.66	3 × 25	75.5
24	5.92	3 × 25	78.9
25	5.86	3 × 25	78.1
26	5.98	3 × 25	79.7
27	5.96	3 × 25	79.5
28	5.98	3 × 25	79.7
			Average velocity=82.1

Because the conditions of the model test have some difference from that on the numerical calculation at Part 1, the numerical simulation was carried out again with model test conditions. Table 10 gives the information on the comparison of the measurements with the CFD modeling at the same conditions and the magnitude of velocity is a statistic average magnitude.

**Table 10.**  
**Comparison of the measurement results with CFD modeling data**

Nozzle	Pressure, psi	Velocity, m/s (measurements)	Velocity, m/s (CFD modeling)	Deviation
Circular nozzle	65	48.8	54	10.0%
Circular nozzle	83	58.3	64	9.8%
Rectangular	65	82.1	91	9.9%
Rectangular	82	112.0	101	10.0%

As evidenced in Table 10, the deviation of the experimental results from the modeling data is within  $\pm 10\%$ . Therefore, the model chosen for the numerical simulation was correct. Figure 28 shows the whole test section for particle velocity measurement. Figures 29~33 show the particle imaging from the experimental process at different nozzles and flow pressure. Among these figures, Figure 32 and Figure 33 are used to find the particle concentration distribution. These two figures show that the particles almost fill in the rectangular nozzle blasting area. Therefore, the rectangular nozzles work efficiently.

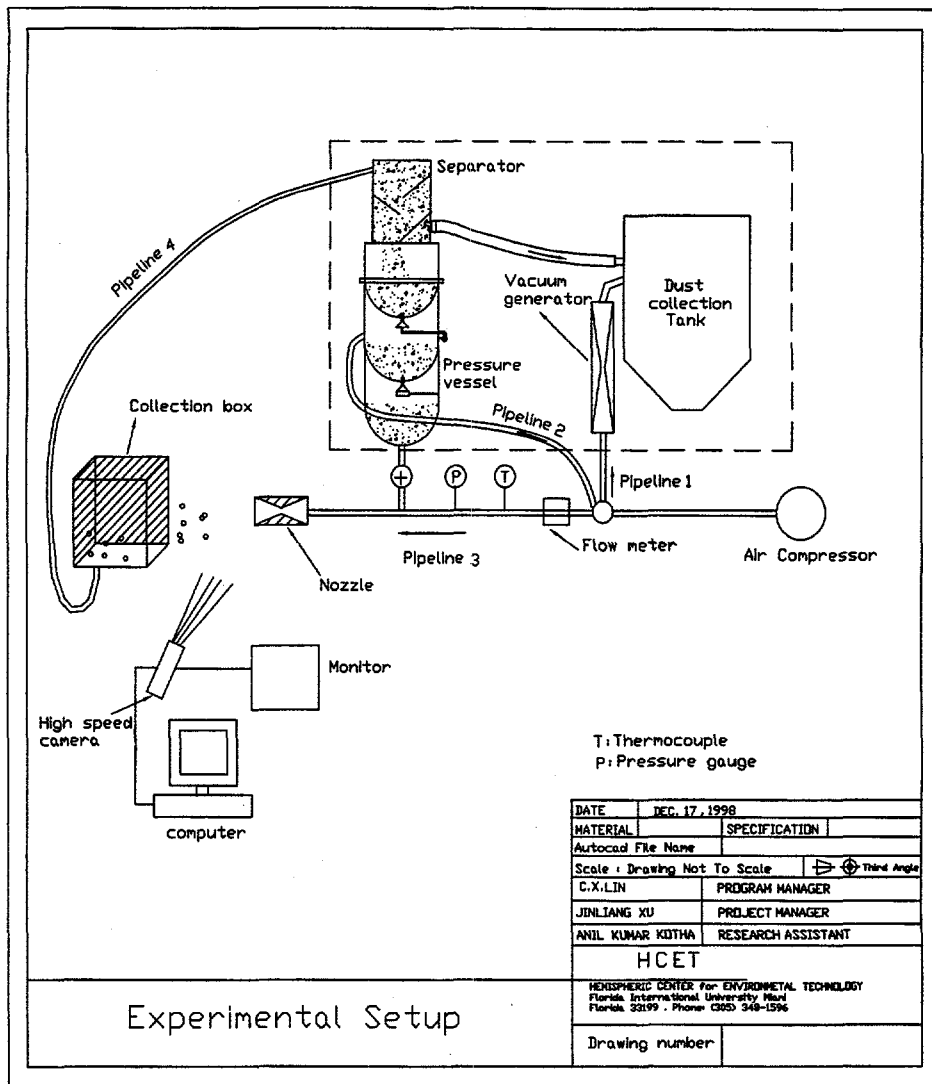


Figure 23. Experimental setup of particle velocity and concentration measurement of the blasting nozzle.



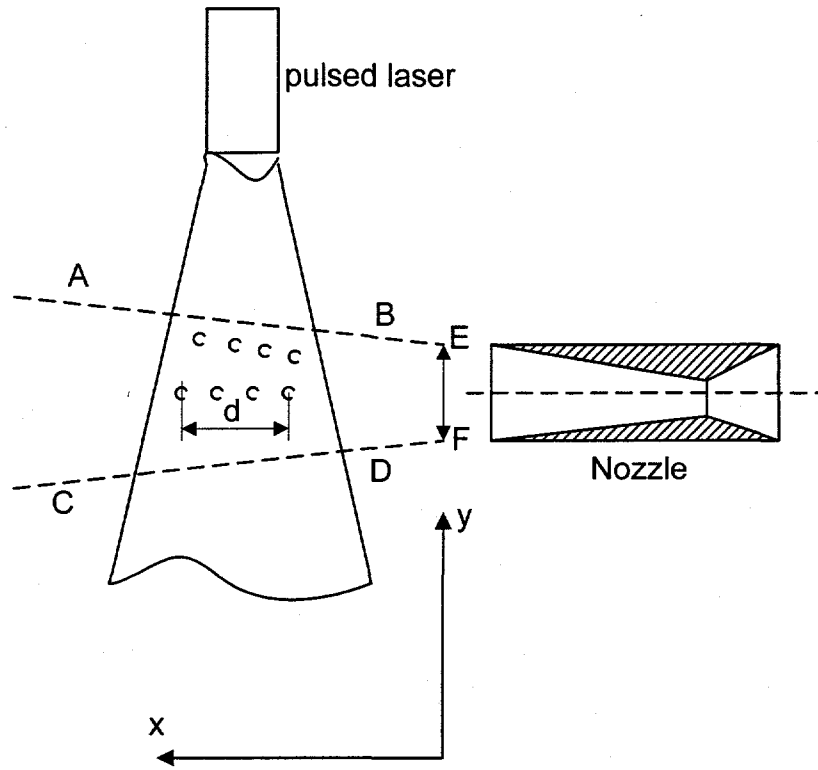


Figure 24. Measurement mechanism of the particle velocity and concentration.

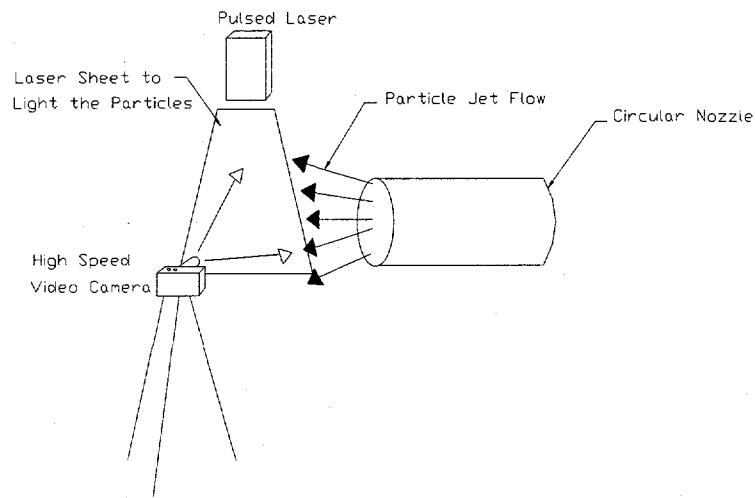


Figure 25. Measurement arrangement for the existing circular nozzle with 1/4 inch throat diameter.

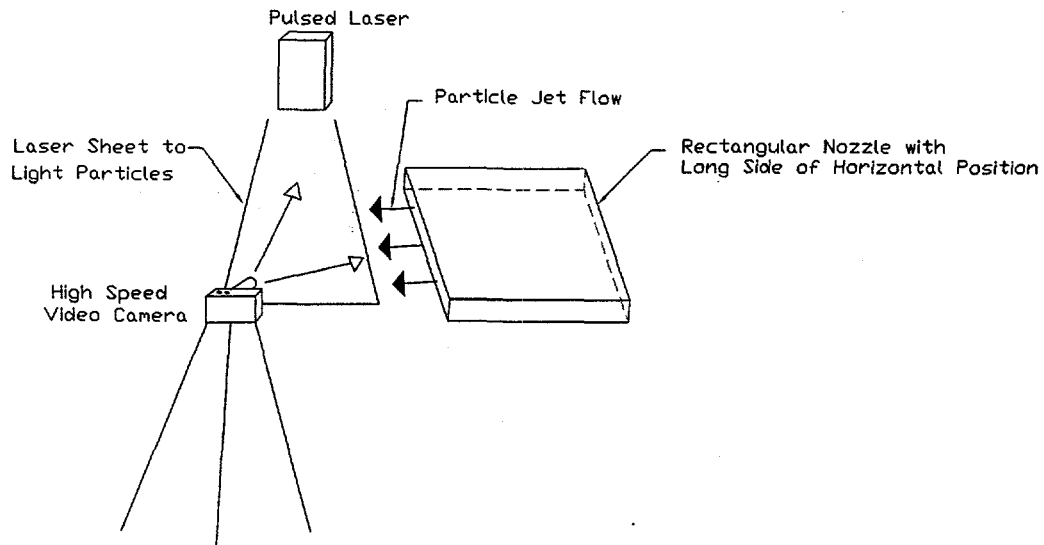


Figure 26. Measurement arrangement for the new rectangular nozzle with long side at horizontal position.

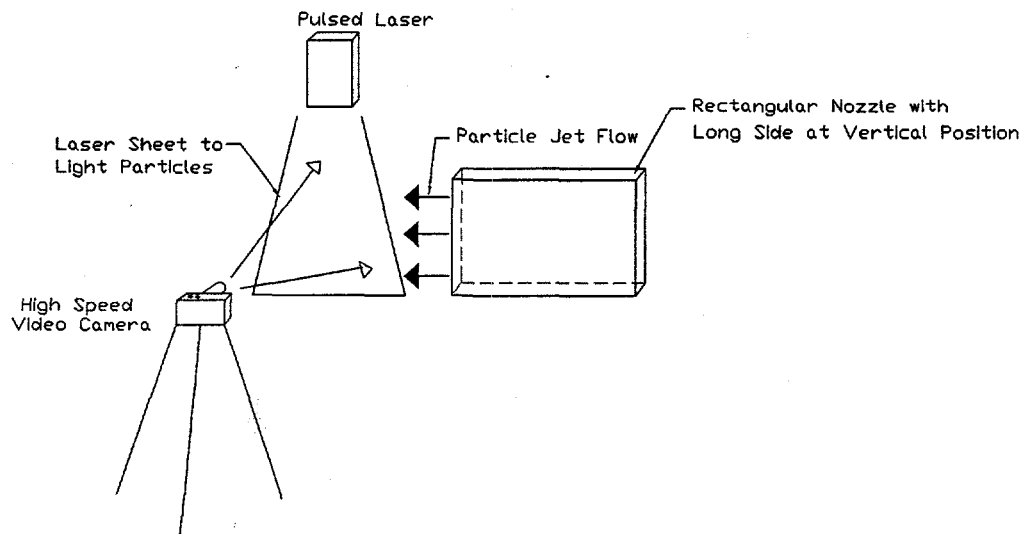


Figure 27. Measurement arrangement for the new rectangular nozzle with long side at vertical position.

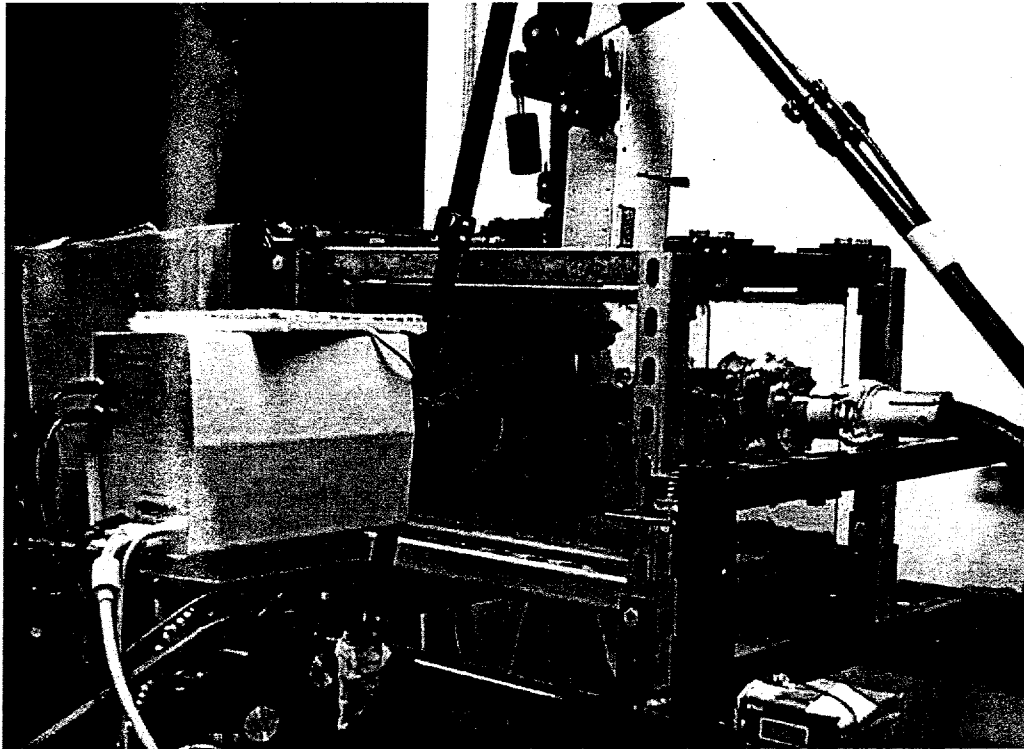


Figure 28. The test section for measuring blasting nozzle velocity and construction.

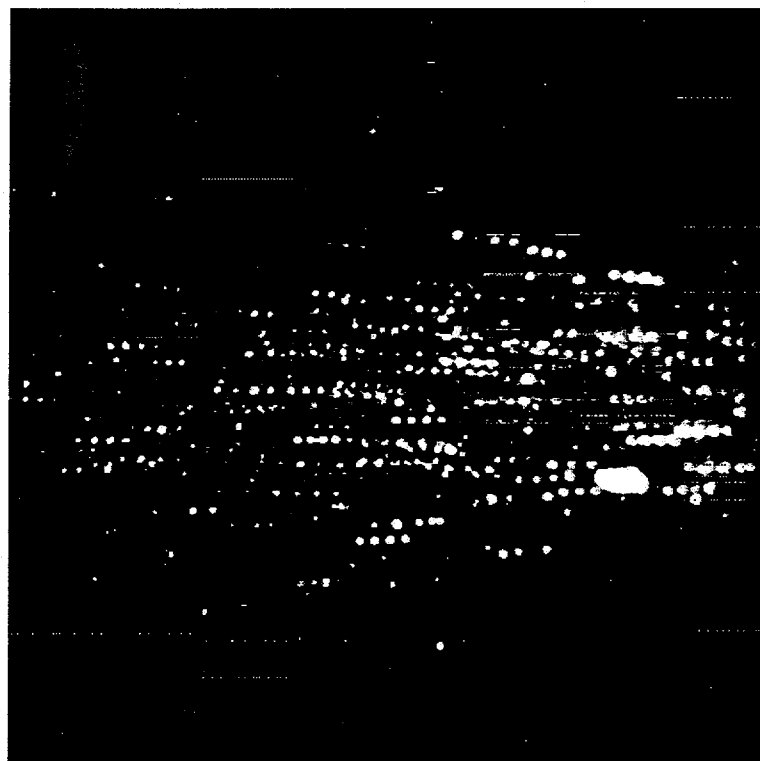


Figure 29. Particles imaging for circular nozzle at P =83 psi.

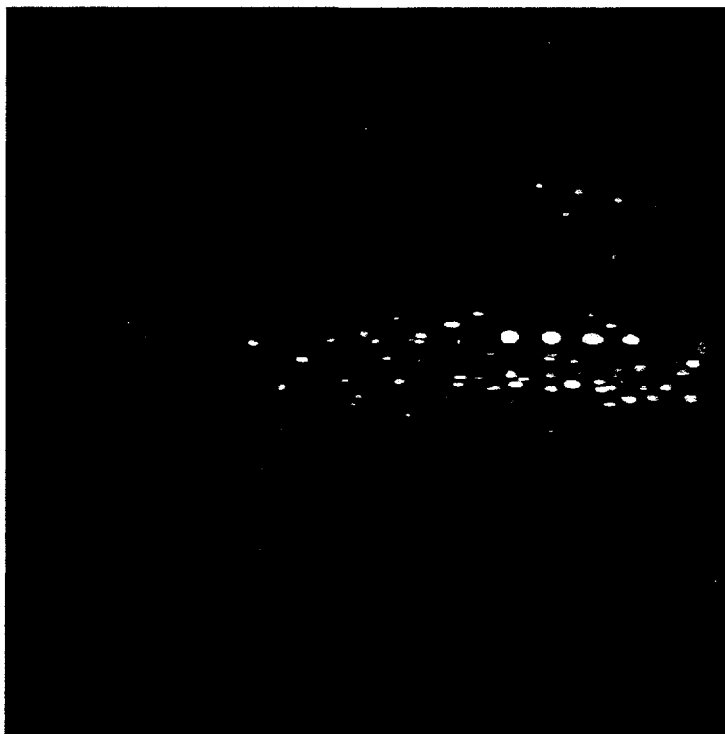


Figure 30. Particles imaging for rectangular nozzle at P = 82 psi (nozzle orientation, see Figure 26).

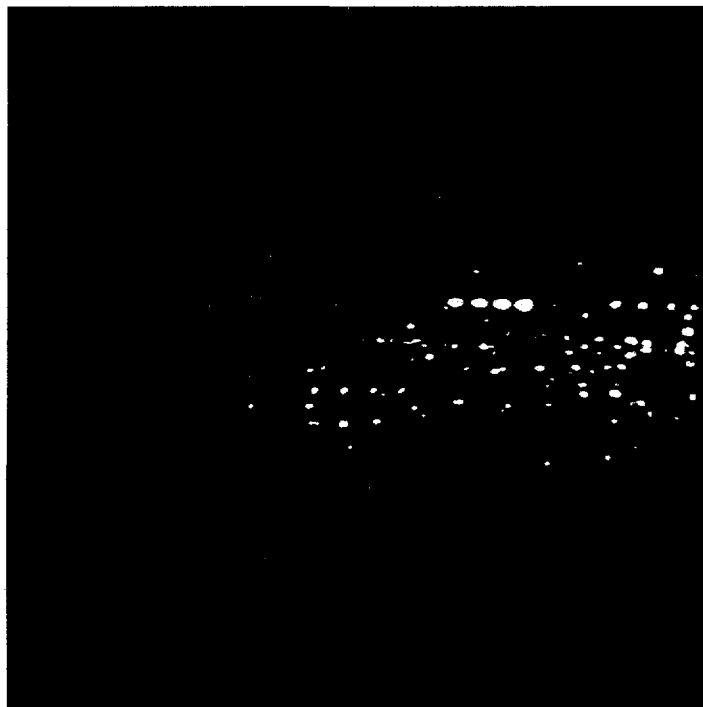
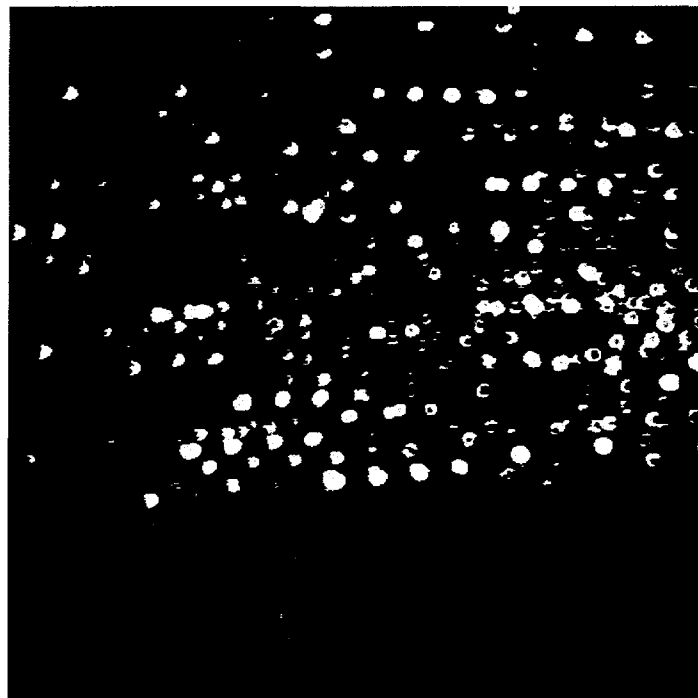


Figure 31. Particles imaging for rectangular nozzle at P = 65 psi (nozzle orientation, see Figure 26).



**Figure 32. Particles imaging for rectangular nozzle at P =82 psi (nozzle orientation, see Figure 27).**



**Figure 33. Particles imaging for rectangular nozzle at P =65 psi (nozzle orientation, see Figure 27).**

## 3.2 Centrifugal separator test results

### 3.2.1 Efficiency test

On April 30, the test of the new separator's separation efficiency was carried out for the same working conditions as the nozzles test (see Figure 34). The experiment procedure was as follows.

First, the new separator was fed by two kinds of dust obtained from the existing separator. The two kinds of dust were classified as concrete dust and coating dust. Second, the new separator's dust and recycle grit, which were collected with plastic bags, were weighed. The two different working conditions produced the following results:

1. For concrete wall surface, we obtained 84.1% recycle grit from the dust of the existing separator (a total of 796.4g dust was fed to the new separator. We got 126.4g pure dust and 670.5g recycle grit.). The efficiency of the existing separator for this condition was 25%.
2. For coating on steel plate surface, we obtained 73.5% recycle grit from the dust of the existing separator (90.5g dust was fed to the new separator. We got 24.0g pure dust and 66.5g recycle grit.). The efficiency of the existing separator for this condition was 30%.

The above results prove the almost doubled efficiency and the improved separation efficiency to perfect status.

Similar to the blasting nozzle, the numerical simulation was carried out on the centrifugal separator again at the model test condition. Compared with the experimental result of this centrifugal separator, the difference between numerical and experimental results is below  $\pm 10\%$  (75% from numerical modeling data for this case; 84.1% and 73.5% from experimental results mentioned above). Table 11 lists all the comparison results.

**Table 11.**  
Comparison of the measurement results with CFD modeling data

	Efficiency (CFD modeling)	Efficiency (test data)	Deviation
Existing separator	27%	25% (for concrete surface)	5%
		20% (for coating on steel plate surface)	10%
Newly designed centrifugal separator	75%	84.1% (for concrete wall surface)	10%
		73.5% (for coating on steel plate surface)	5%

### 3.2.2 Velocity Distribution Test

In order to verify the modeling results, two different positions were chosen to obtain the new separator's internal velocity distribution. On May 4, the test was accomplished. The experimental procedure is reported below.

Two ½ inch holes were drilled on the external surface of the separator. One is 2" and the other is 6" from the separator's top surface. The holes are on the opposite side surface of the separator's tangential air inlet channel. Two directional (tangential direction along the cylinder surface and axial along the vertical direction) velocities were measured to compare with the numerical simulation results. A 6060P Pitot probe from ALNOR INSTRUMENT COMPANY was employed to obtain the velocity distribution.

Figure 34 is a picture of the new centrifugal separator. In the picture, two probe holes, sealed with tape, can be seen clearly. Figures 35 to 38 show the results from experimental and numerical modeling. The direction of coordinates begins from the centerline of the separator to the air inlet channel surface. For the upper hole, since it was in the middle of two concentric cylinders, the distance is much shorter than that for the other position. Judging from these figures, the distinction of the experimental results and the estimated data agree fairly well with a deviation within  $\pm 10\%$ . Therefore, it can be assumed that the numerical model and the newly designed separator are successful.

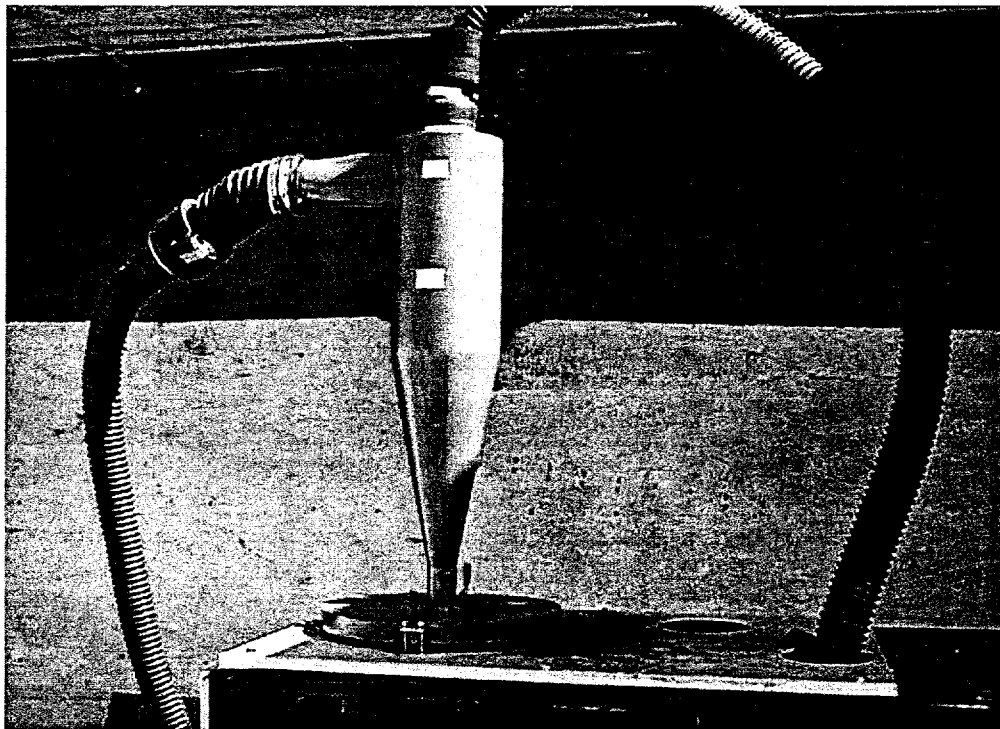


Figure 34. Picture of the new centrifugal separator.

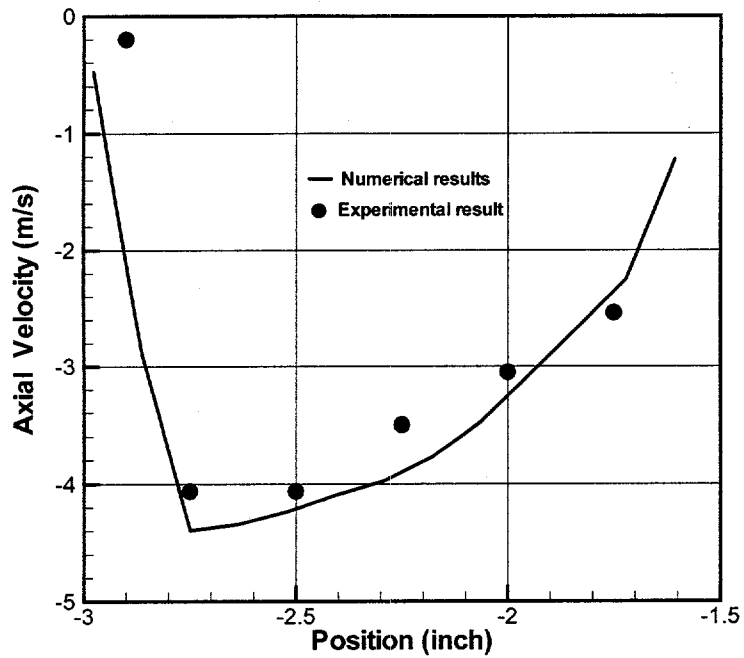


Figure 35. Comparison of numerical results and experiment data in the axial direction at the upper position (i.e., 2" to the separator's top surface).

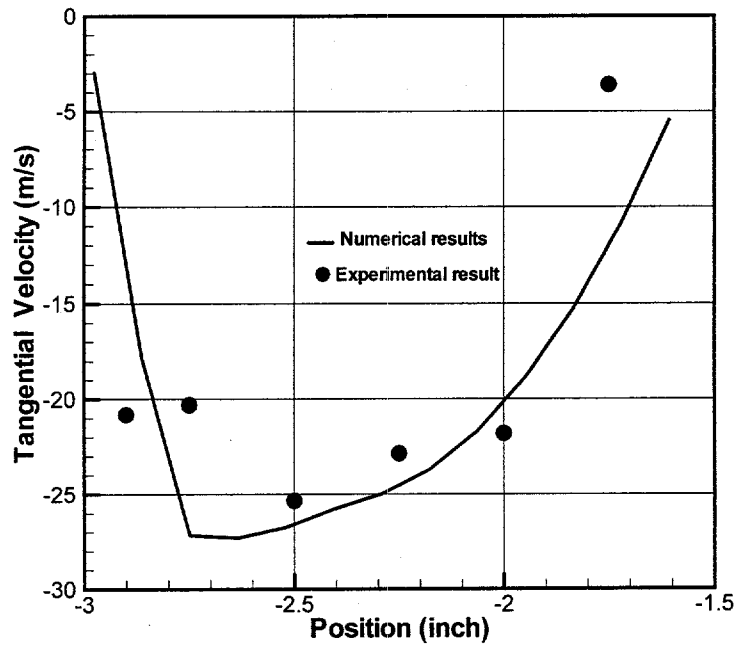


Figure 36. Comparison of numerical results and experiment data in the tangential direction at the upper position (i.e., 2" to the separator's top surface).



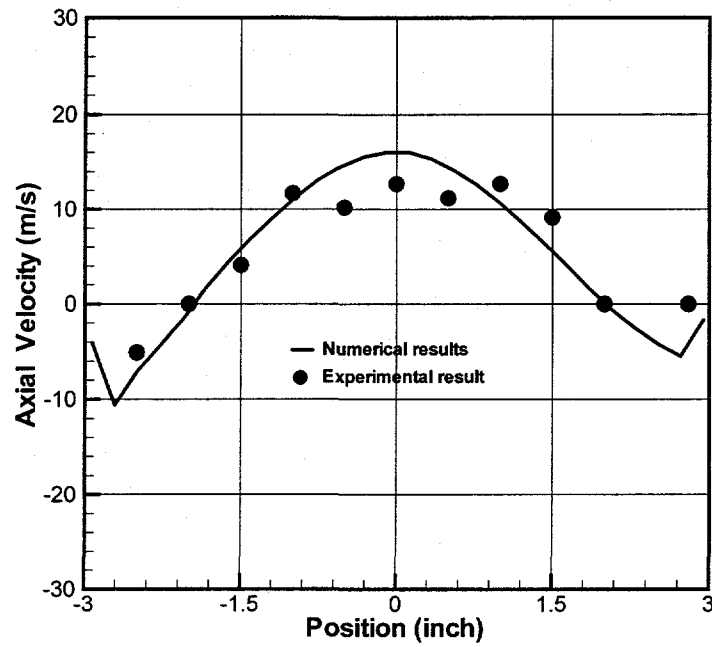


Figure 37. Comparison of numerical results and experiment data in the axial direction at the lower position (i.e., 6" to the separator's top surface).

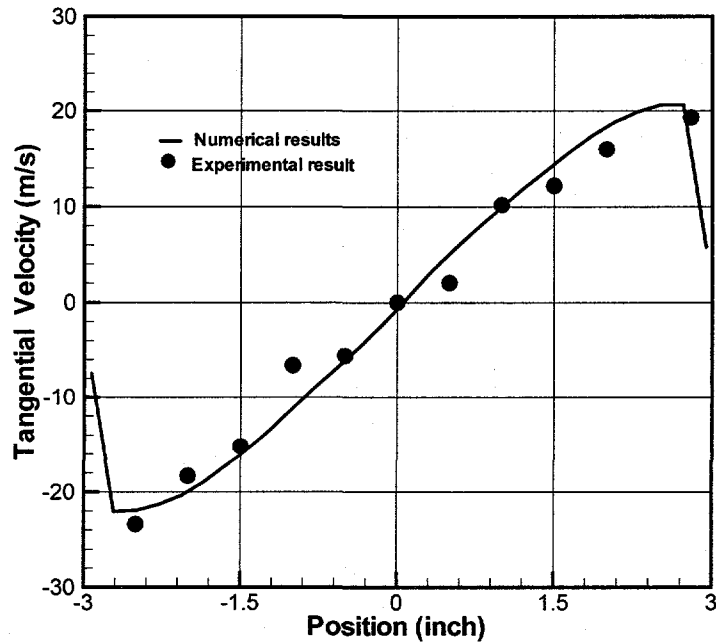


Figure 38. Comparison of numerical results and experiment data in the tangential direction at the lower position (i.e., 6" to the separator's top surface).

## CONCLUSION

---

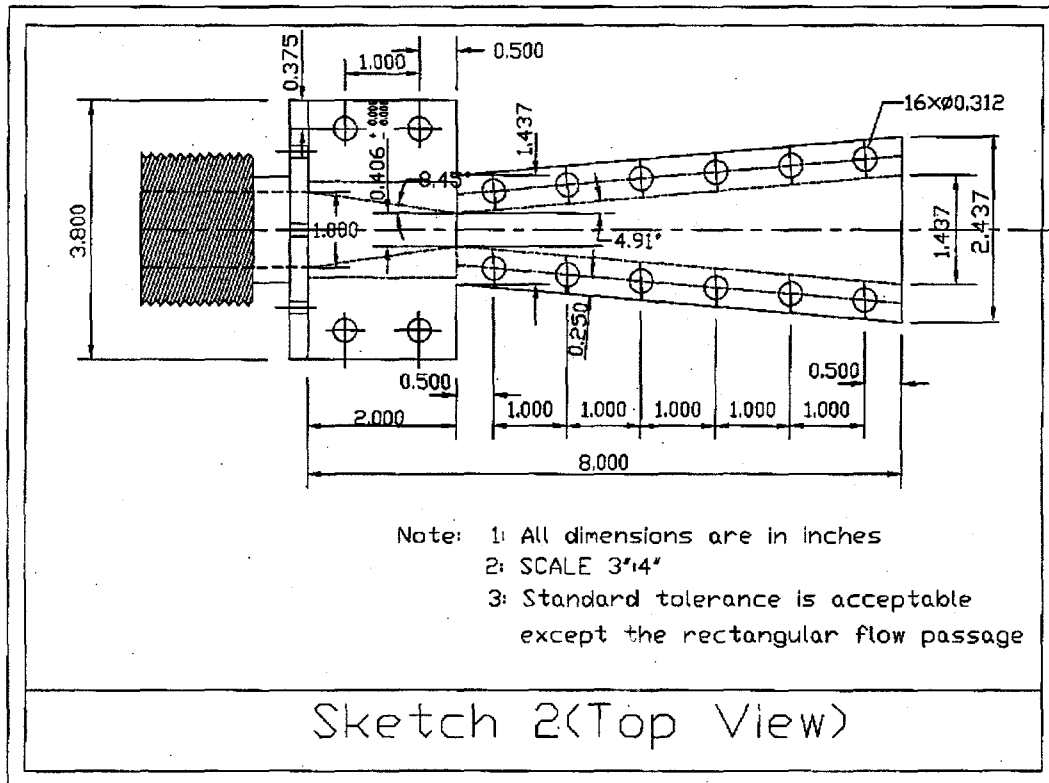
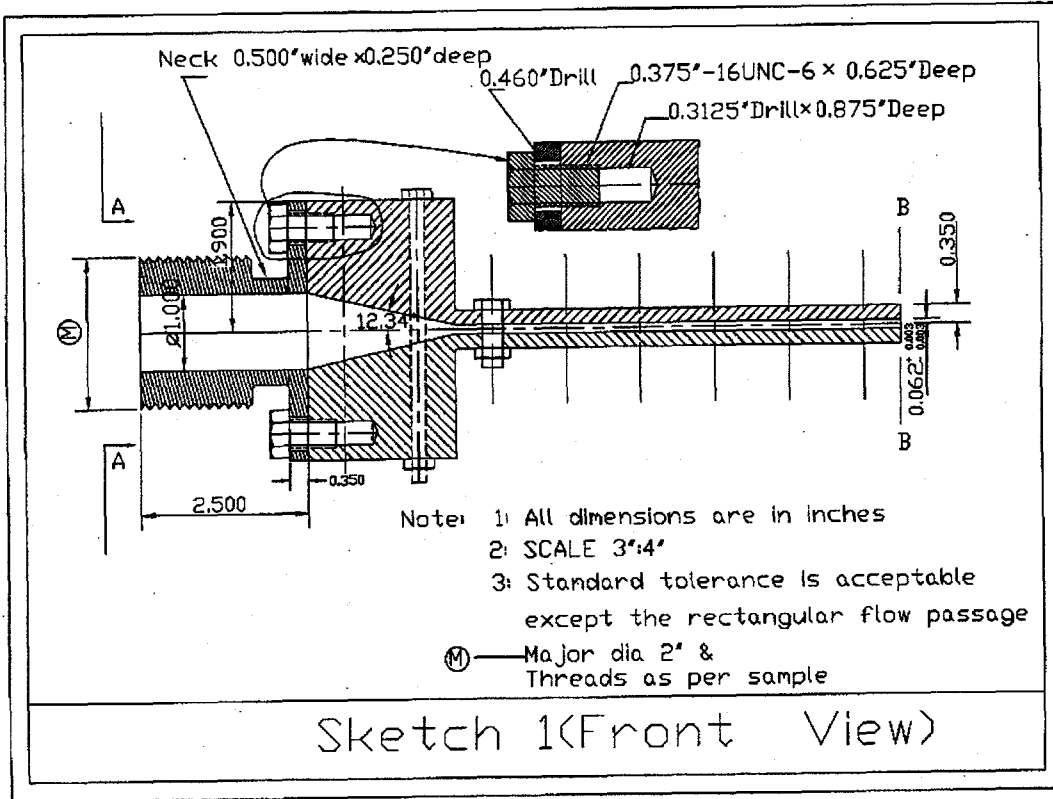
Based on the proposed plan, Phase I has been fulfilled successfully. The main conclusions are as follow:

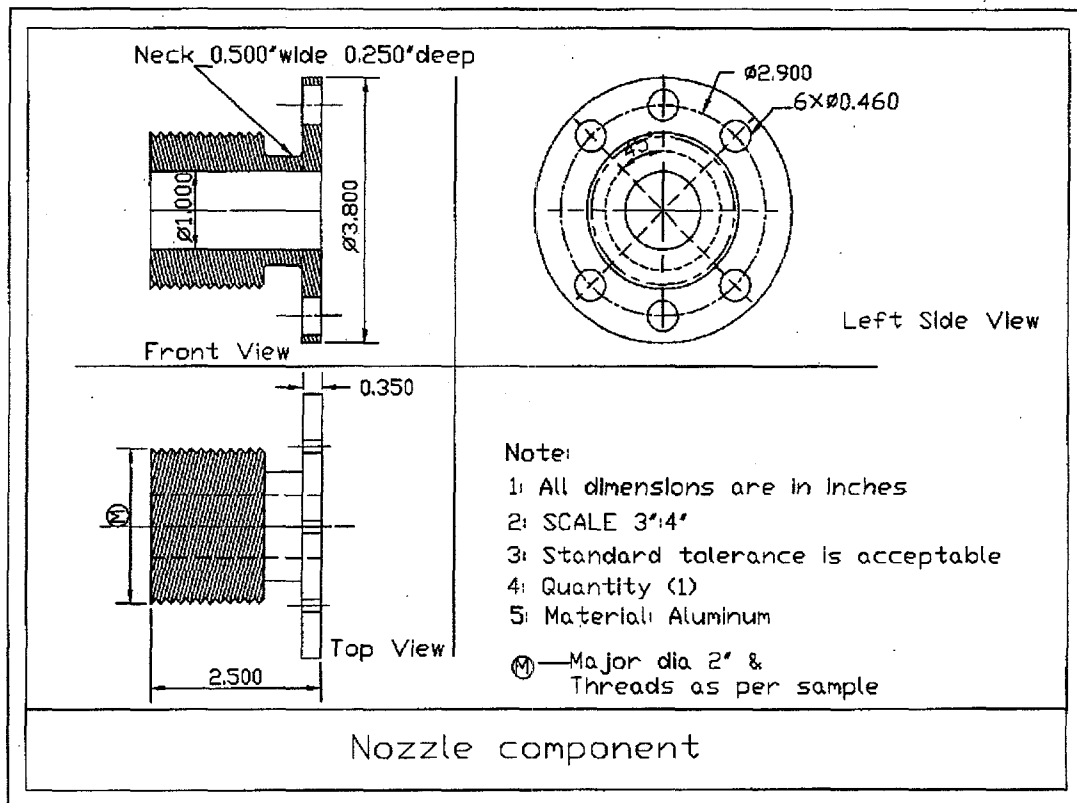
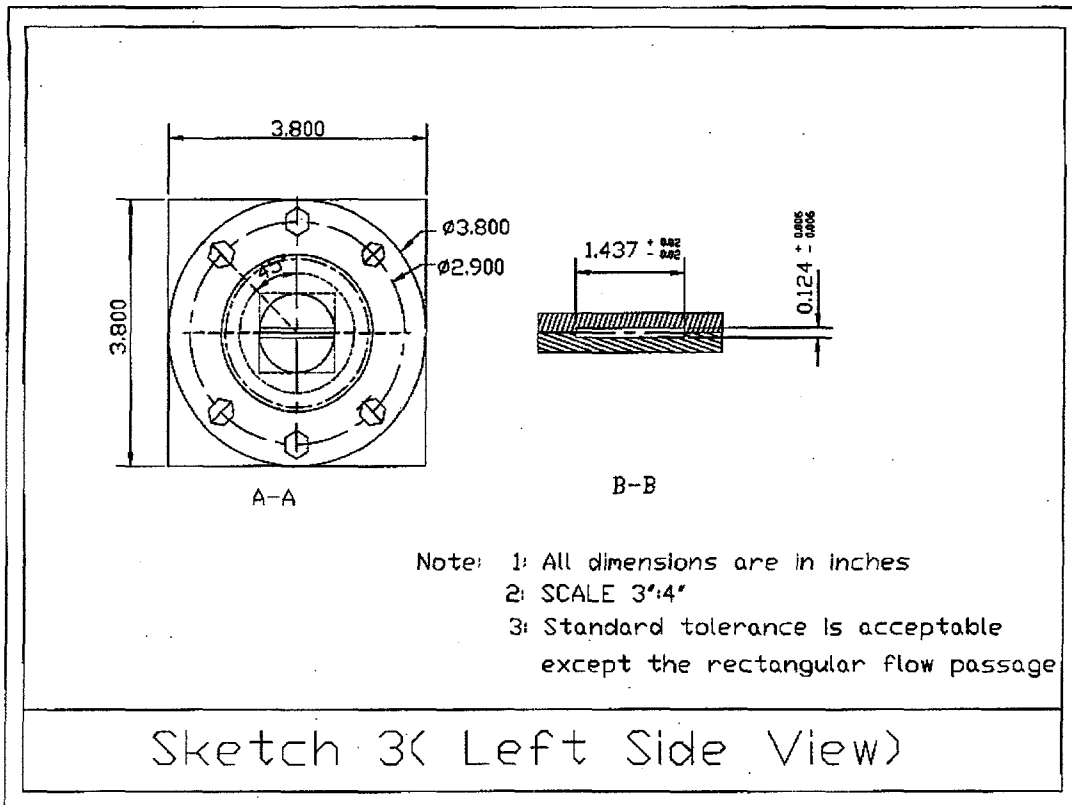
- The numerical modeling on blasting nozzles, including 1) circular and rectangular configuration; 2) the existing separator and newly designed centrifugal separator; and 3) the newly designed blasthead/wind curtain, has been finished.
- The designs of the rectangular blasting nozzle, new centrifugal separator, and blasthead/wind curtain have been finished, based on numerical results.
- The experimental system for the test of particle speed and separator efficiency has been set up. The high-speed video camera system used to measure the particle velocity and concentration has been installed. All the instruments, including pressure gauge, flow meter, thermocouples, and Pitot probe, have been employed in the experimental process.
- The fabrications of the blasting nozzle with  $\frac{1}{4}$  inch equivalent throat diameter, collection box, centrifugal separator, and some other equipment have been done.
- Two types of sensor have been proposed. The radiological characterization sensor system will be incorporated into the structure of the blasthead as compactly as possible to minimize the stand-off distance from an adjacent perpendicular surface. The lift-off sensor system will incorporate sensitive differential pressure switches/transducers to monitor the generated negative pressure within the blasthead.
- The model tests for nozzle and separator have been performed successfully. The comparisons of model test data for blasting nozzles and the new centrifugal separator have been done. The maximum deviation from the experimental results for the modeling data is within  $\pm 10\%$ . This proves that the mathematical models for simulating air-particle flow in the vacuum blasting system are successful.

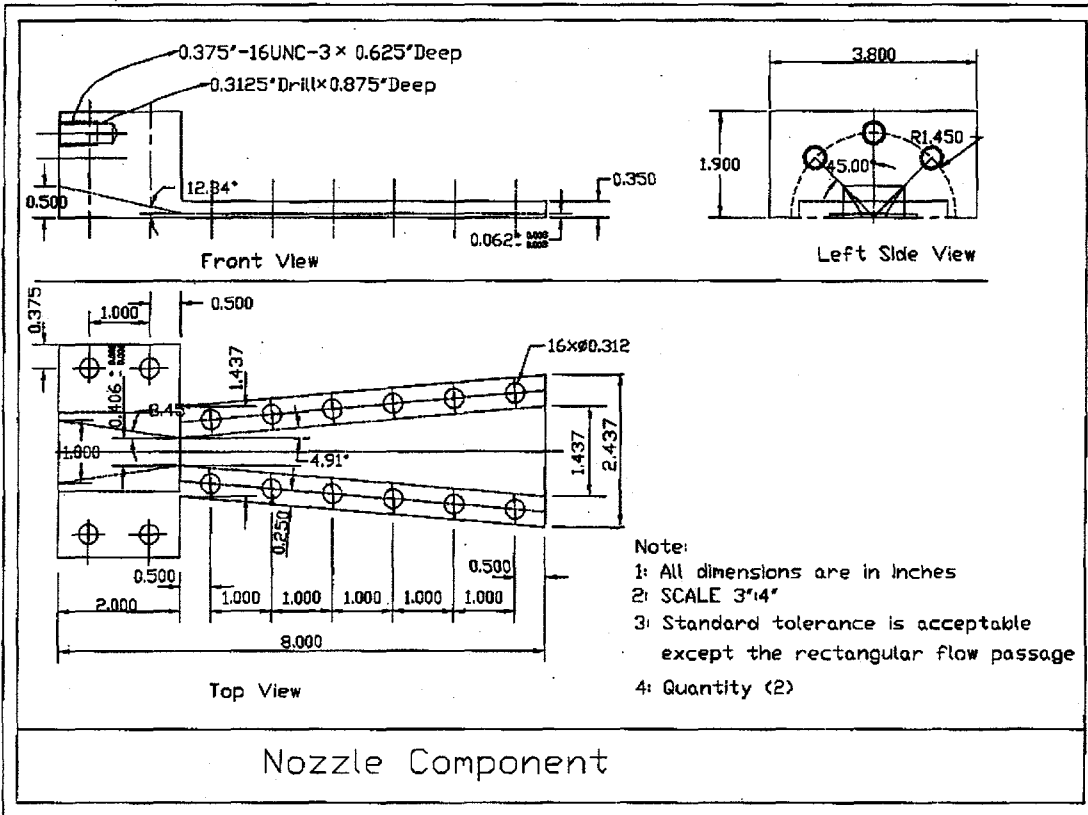
## APPENDIX A

---

### AUTOCAD DRAWING FOR THE RECTANGULAR NOZZLE



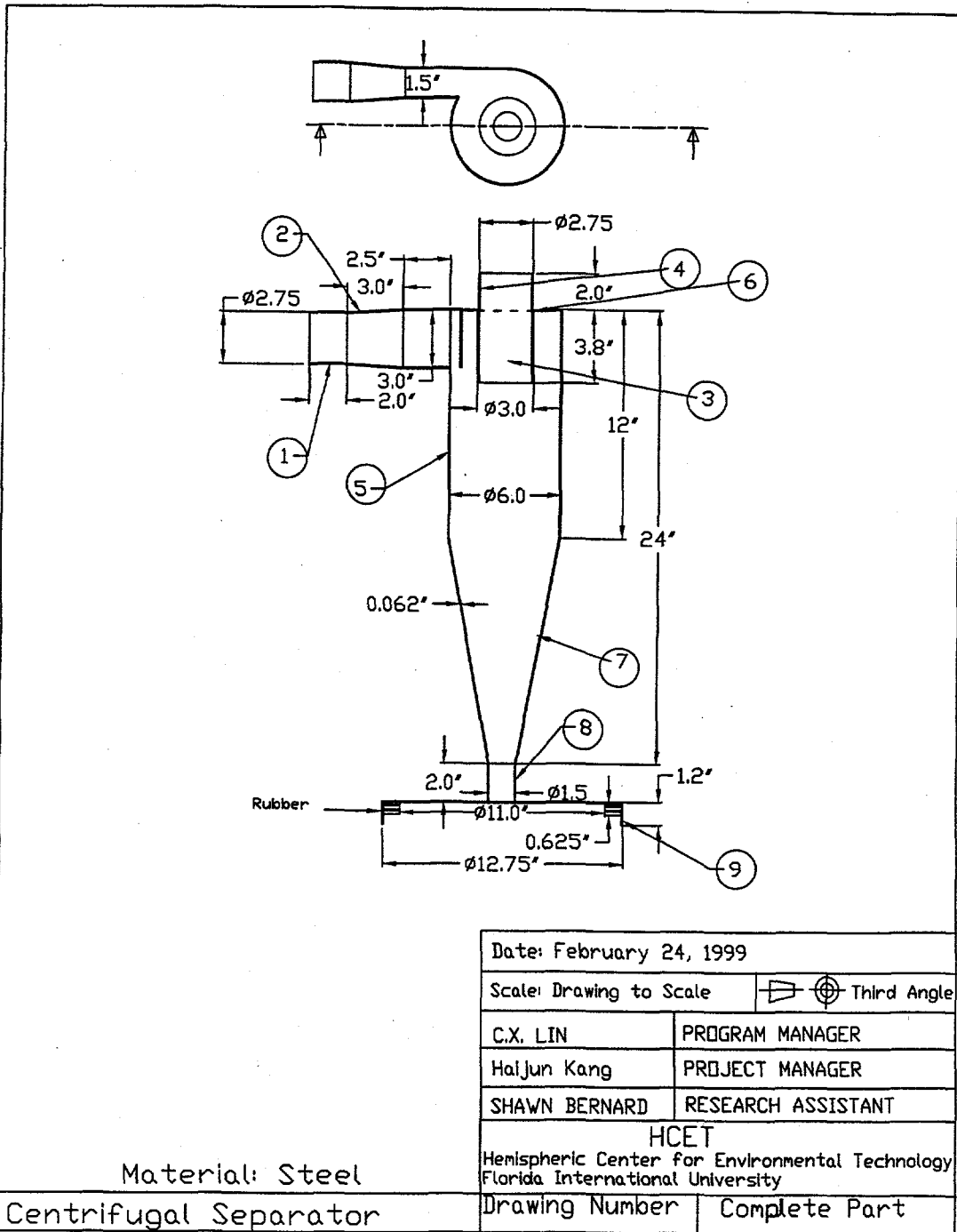




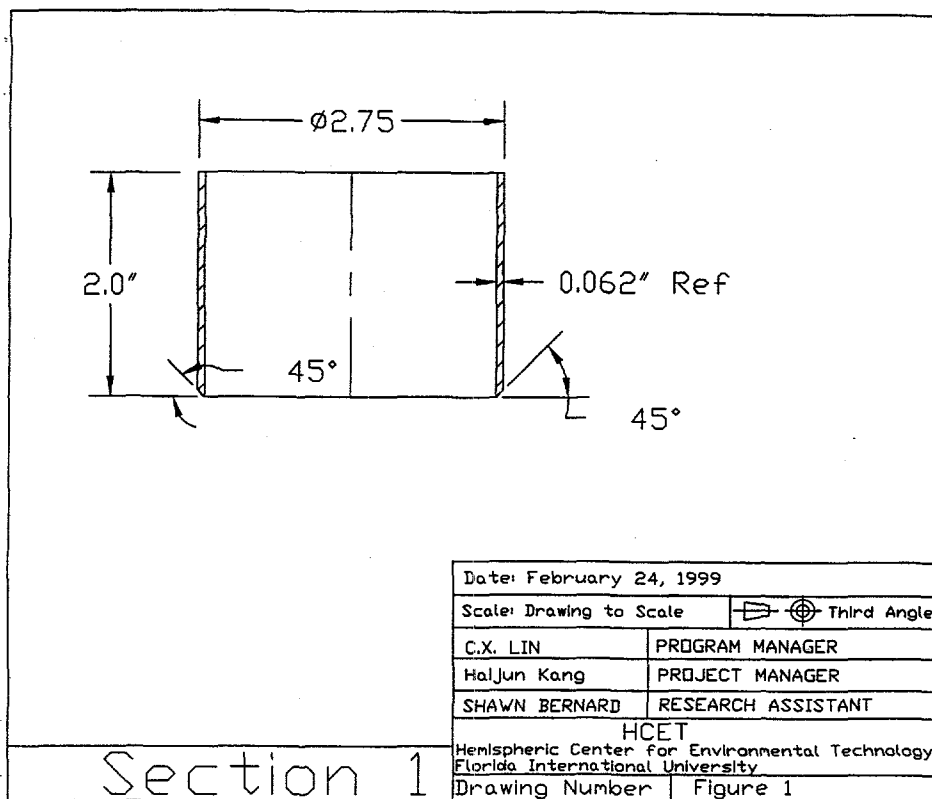
## **APPENDIX B**

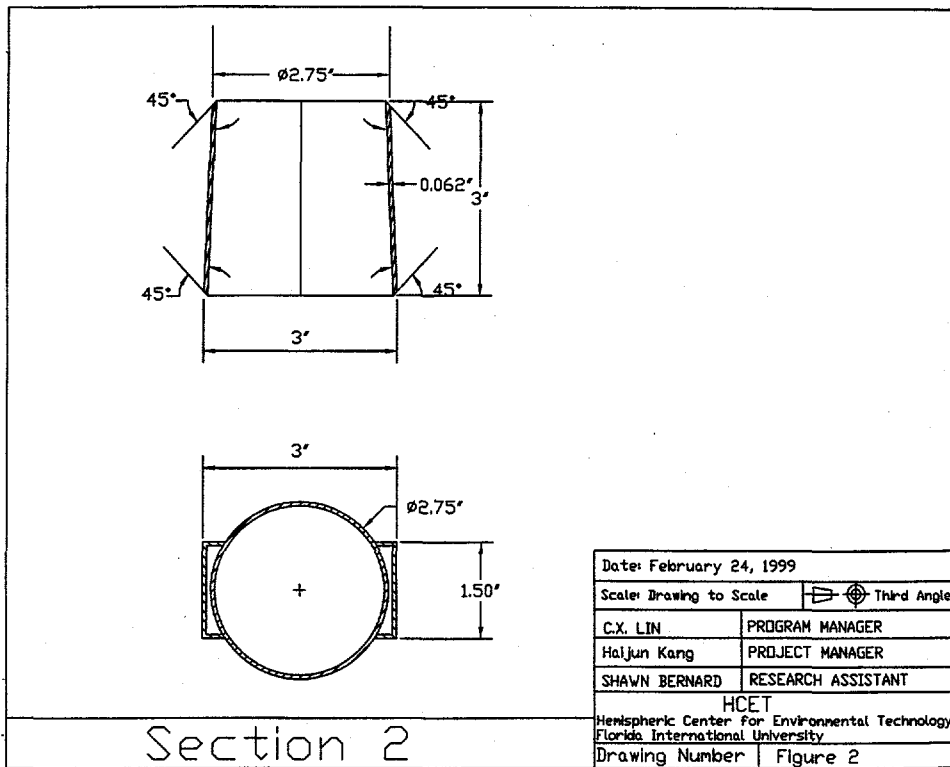
---

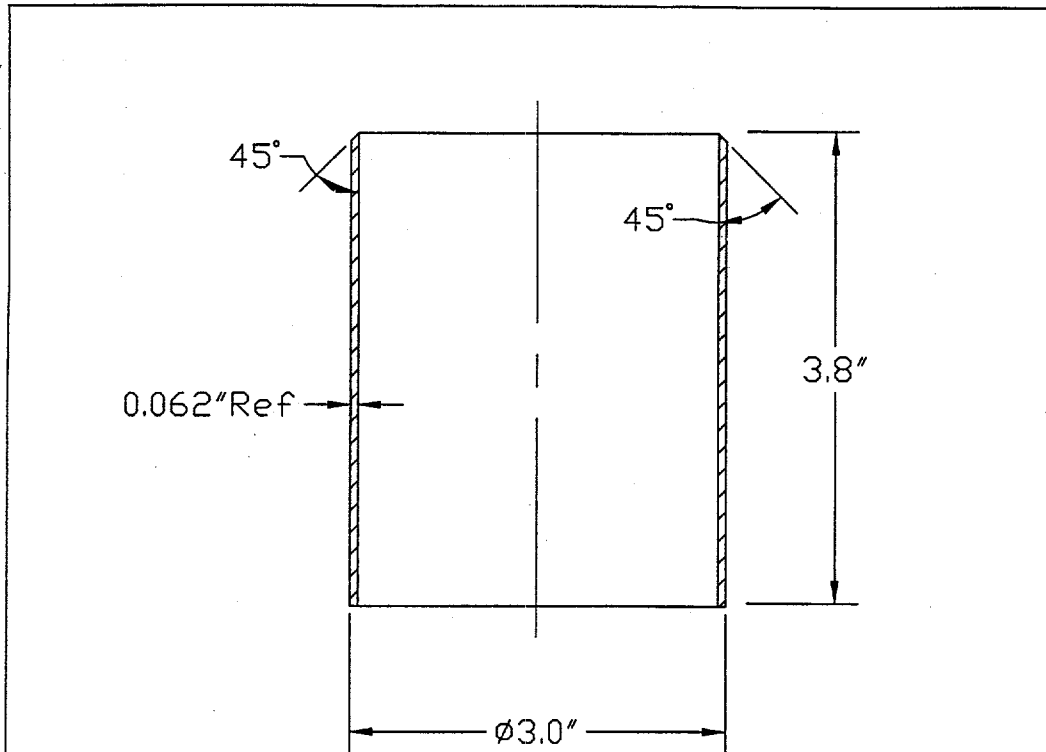
### **AUTOCAD DRAWING FOR THE NEW CENTRIFUGAL SEPARATOR**





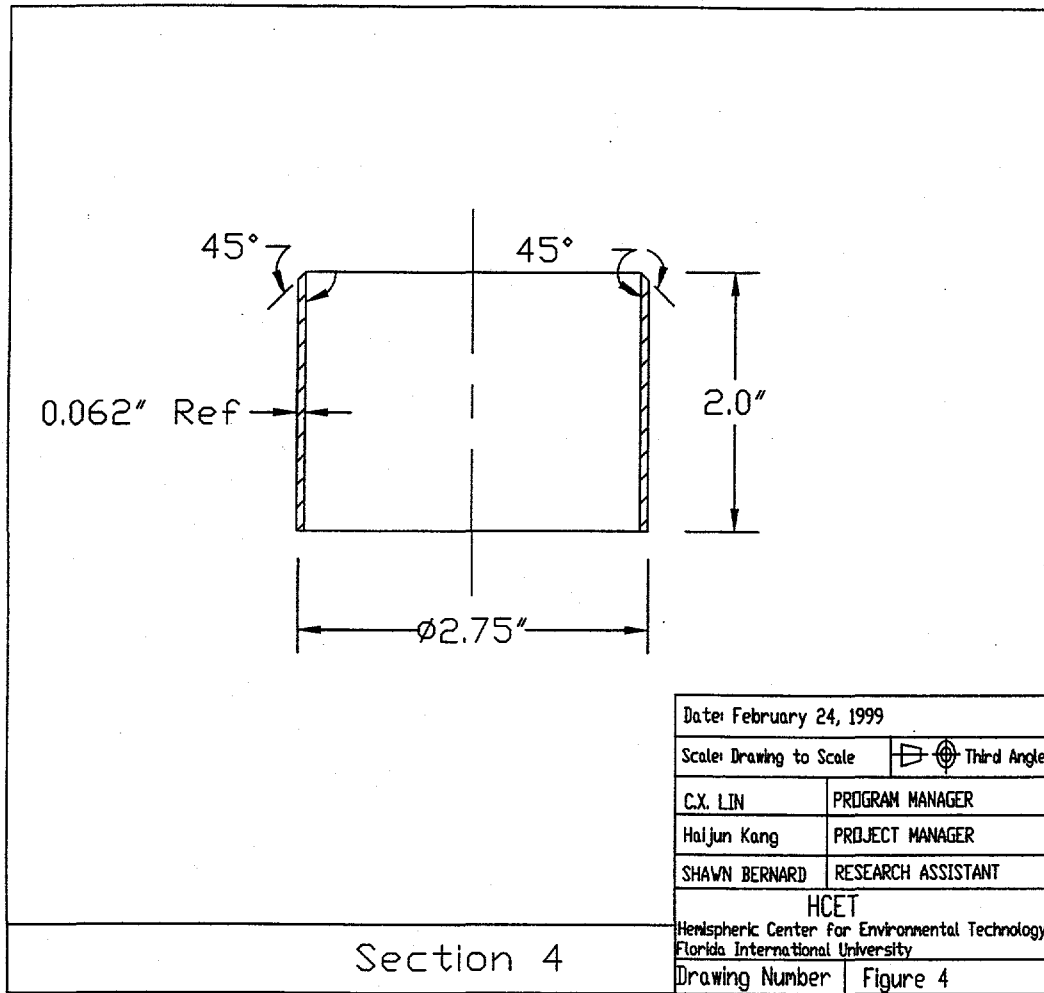


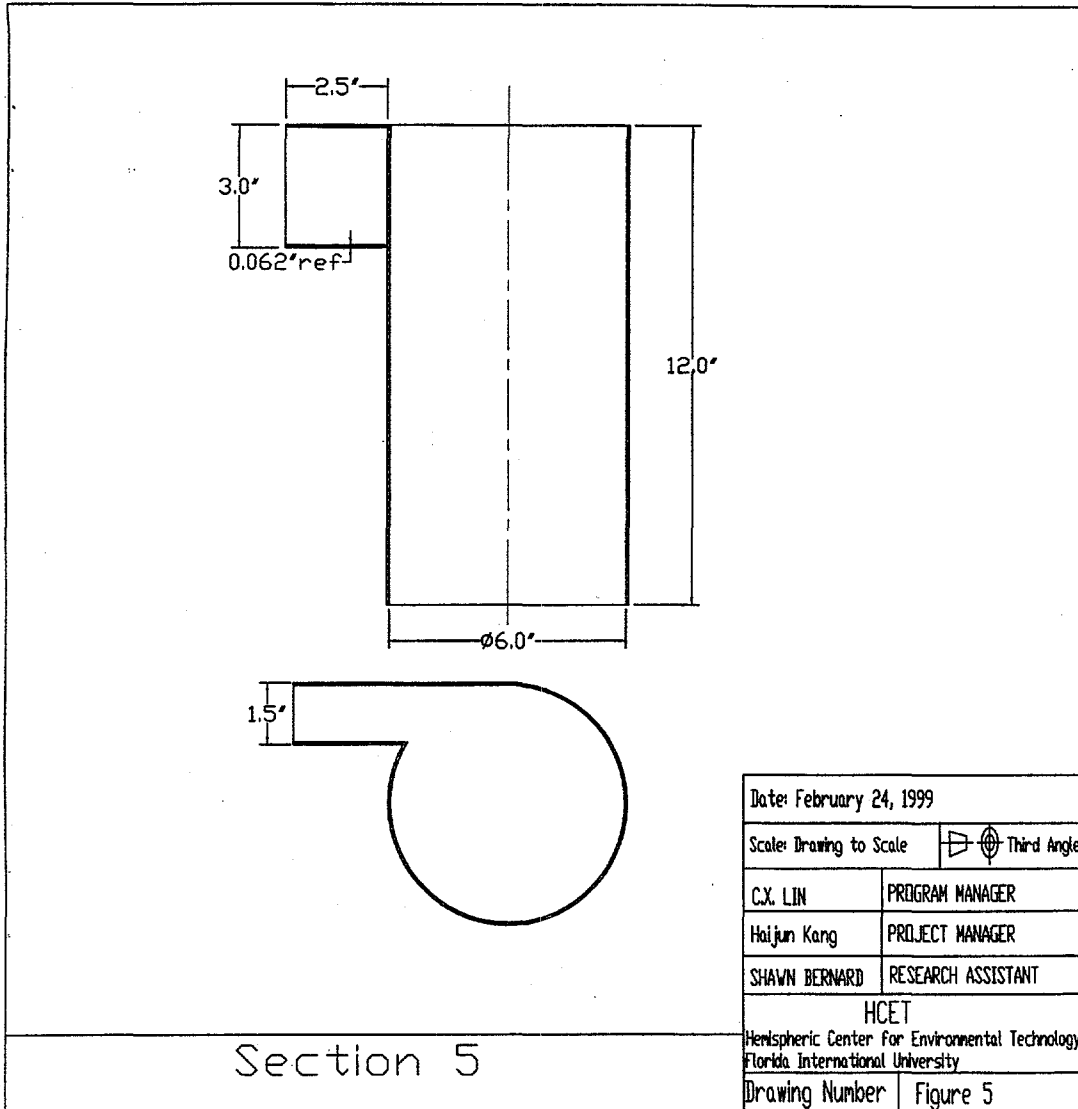


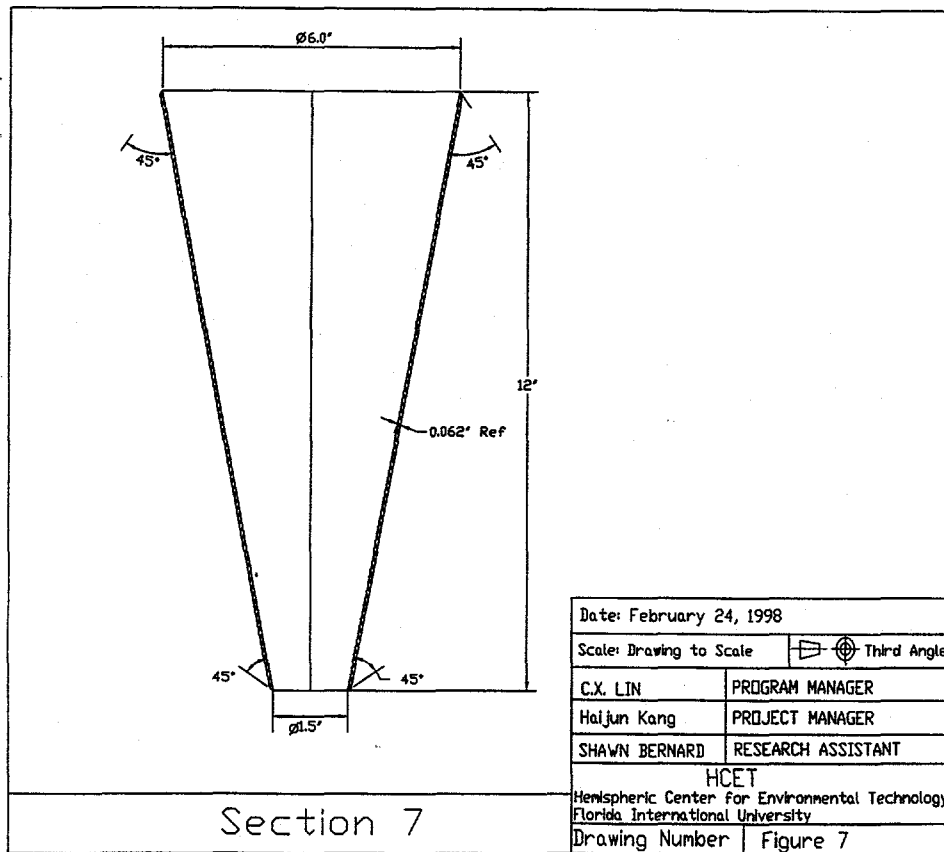
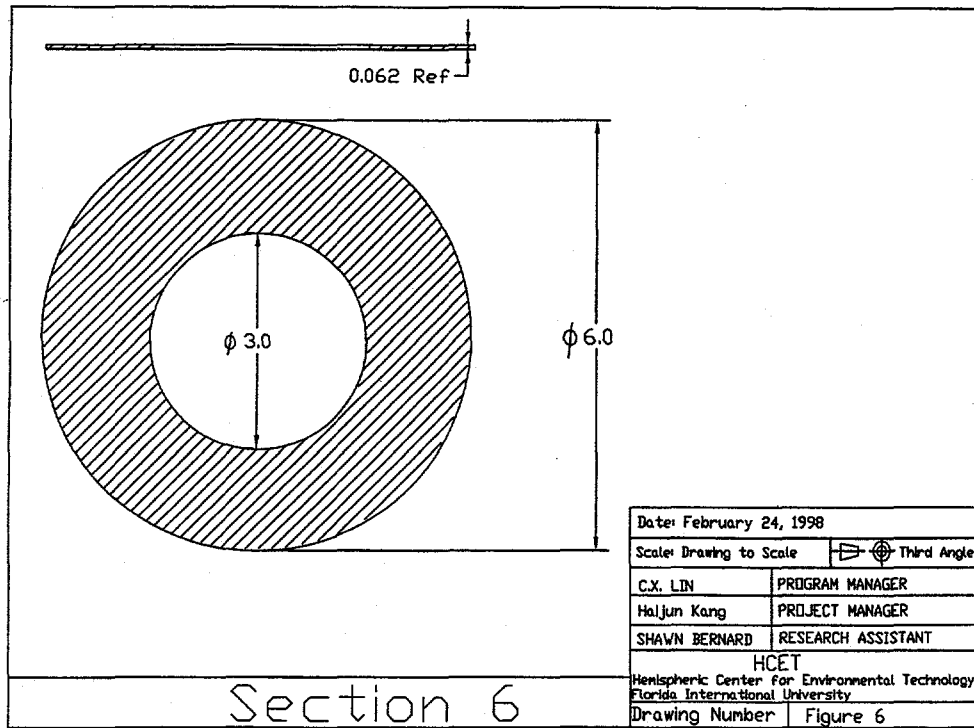


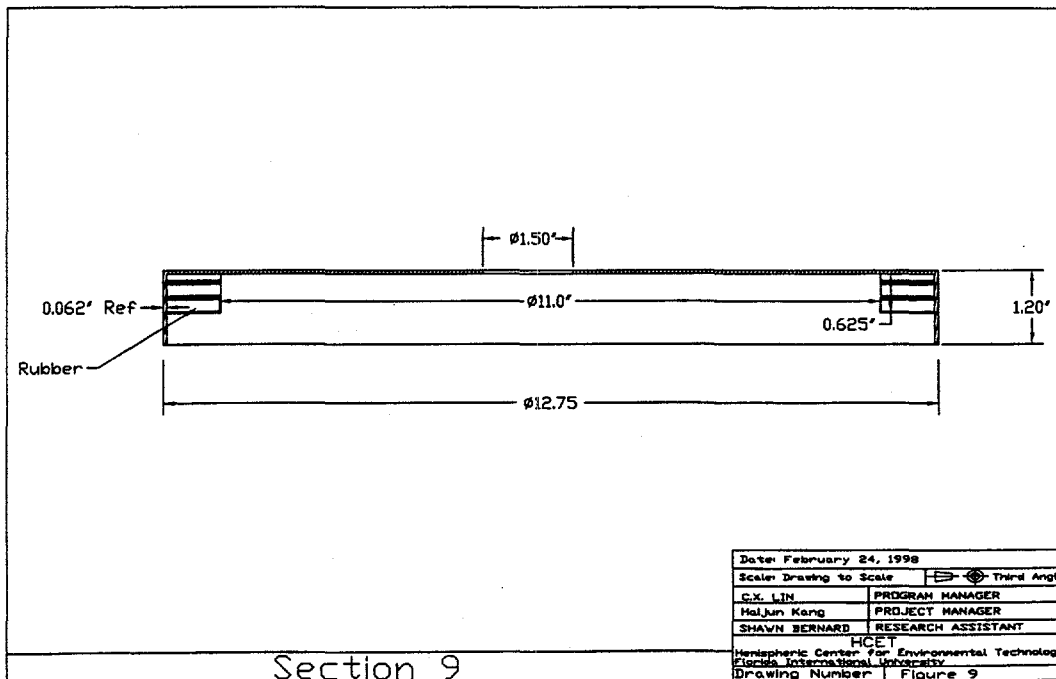
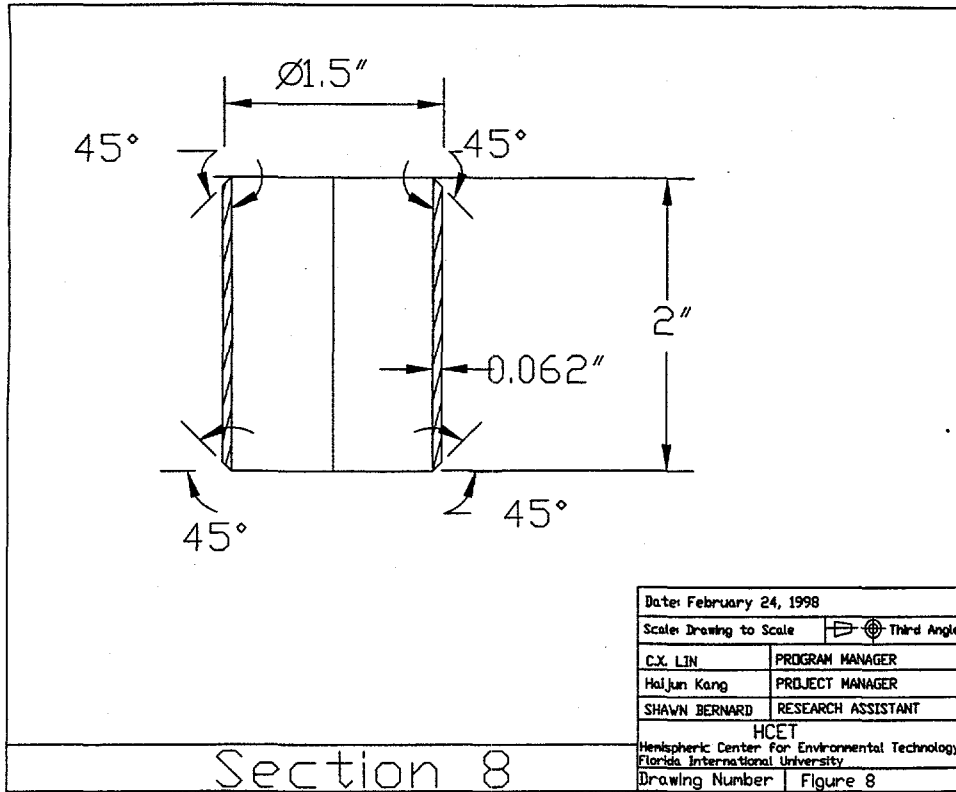
Date: February 24, 1999	
Scale: Drawing to Scale	Third Angle
C.X. LIN	PROGRAM MANAGER
Haijun Kang	PROJECT MANAGER
SHAWN BERNARD	RESEARCH ASSISTANT
HCET	
Hemispheric Center for Environmental Technology Florida International University	
Drawing Number	Figure 3

Section 3







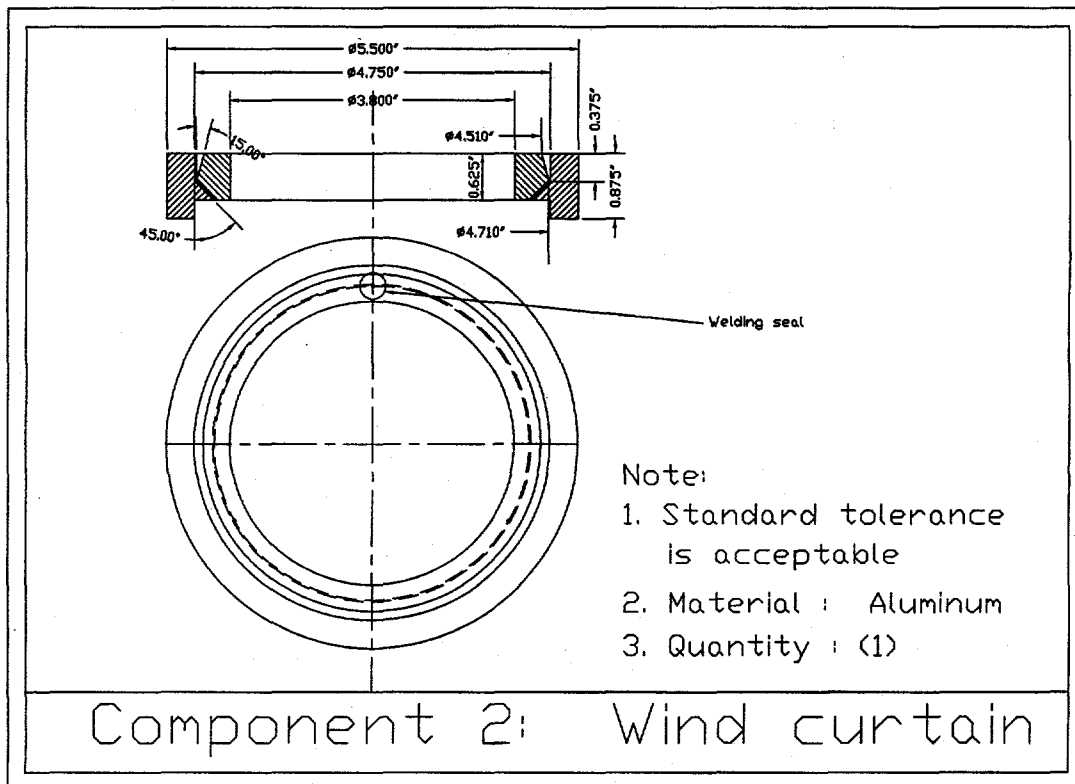
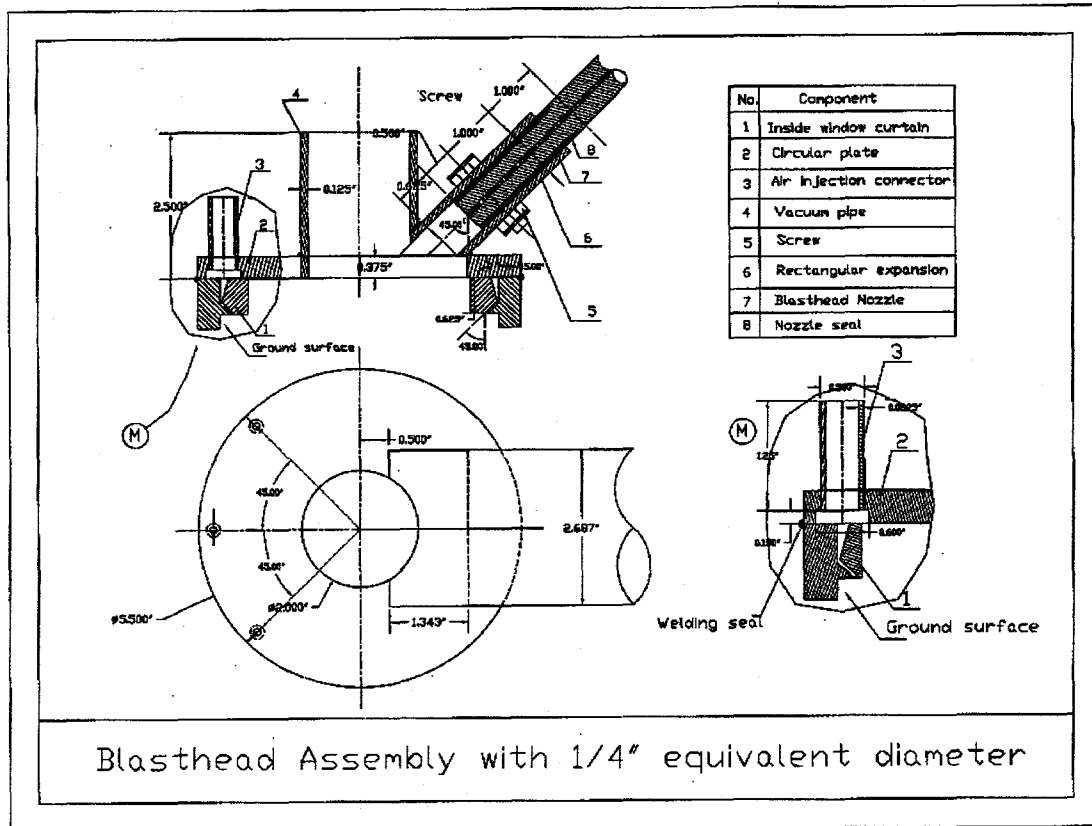


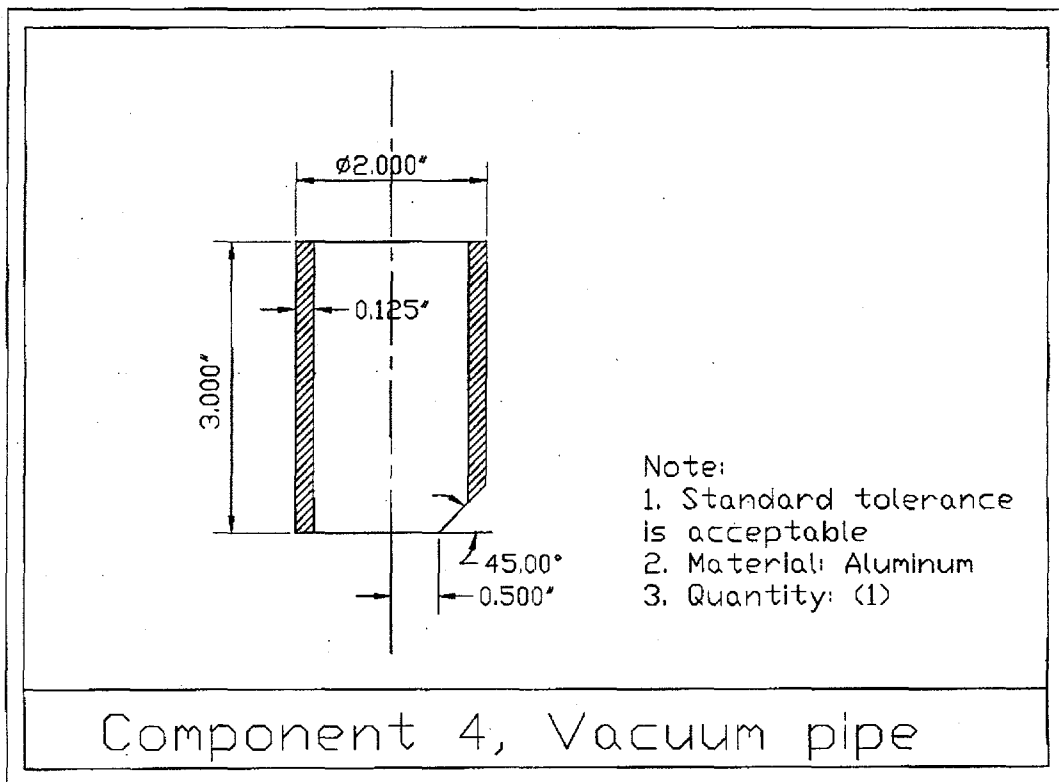
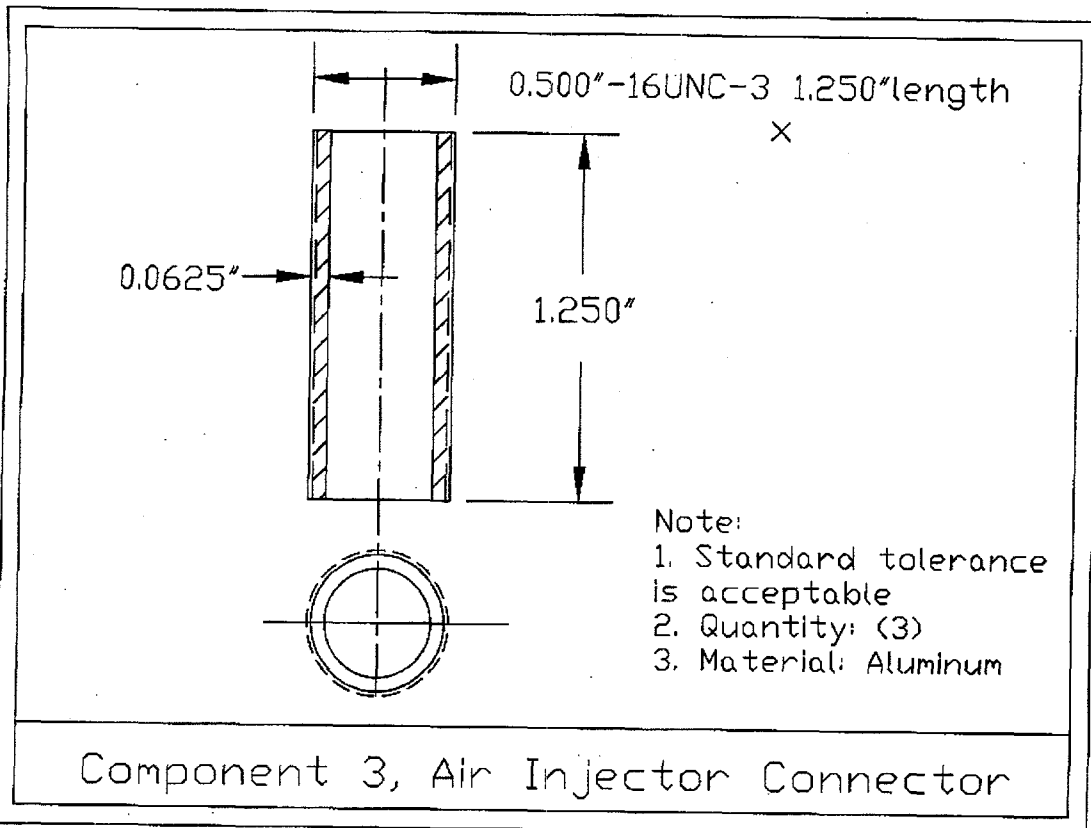
## APPENDIX C

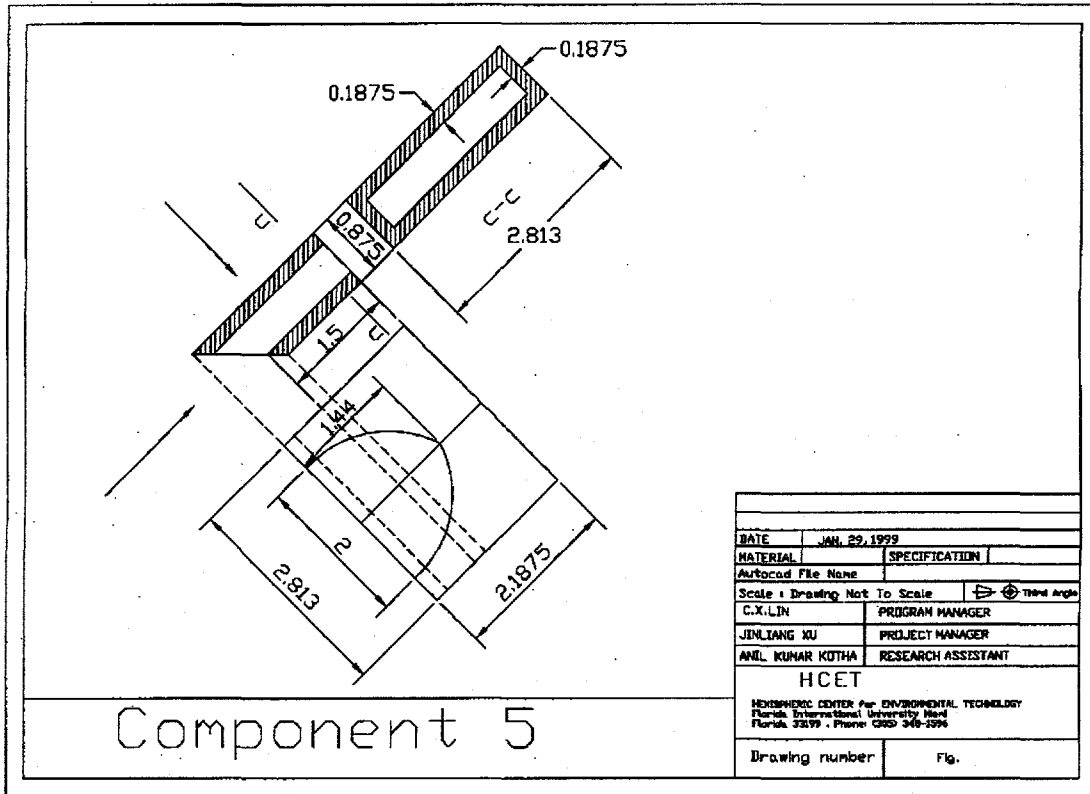
---

### AUTOCAD DRAWING FOR THE WIND CURTAIN









DATE		JAN. 29, 1999	
MATERIAL		SPECIFICATION	
Autocad File Name			
Scale = Drawing Not To Scale		Third Angle	
C.X.LIN		PROGRAM MANAGER	
JINLIANG XU		PROJECT MANAGER	
ANIL KUMAR KOTHA		RESEARCH ASSISTANT	
HCET			
<small>HEMISPHERIC CENTER for ENVIRONMENTAL TECHNOLOGY                  Florida International University Main                  Florida, 33199 • Phone: (305) 348-3396</small>			
Drawing number		Fig.	